Feasibility of Harmonic Motion Imaging Using A Single Transducer: *In Vivo* Imaging of Breast Cancer in A Mouse Model and Human Subjects

Md Murad Hossain, *Member, IEEE*, Niloufar Saharkhiz, *Student Member, IEEE,* and Elisa E. Konofagou, *Member, IEEE*

***Abstract*— Harmonic motion imaging (HMI) interrogates the mechanical properties of tissues by simultaneously generating and tracking harmonic oscillation using focused ultrasound and imaging transducers, respectively. Instead of using two transducers, the objective of this work is to develop a single transducer HMI (ST-HMI) to both generate and track harmonic motion at "on-axis" to the force for facilitating data acquisition. In ST-HMI, the amplitude-modulated force was generated by modulating excitation pulse duration and tracking of motion was performed by transmitting tracking pulses interleaved between excitation pulses. The feasibility of ST-HMI was performed by imaging two elastic phantoms with three inclusions (N=6) and comparing it with acoustic radiation force impulse (ARFI) imaging, *in vivo* longitudinal monitoring of 4T1, orthotropic breast cancer mice (N=4), and patients (N=3) with breast masses *in vivo*. Six inclusions with Young's moduli of 8, 10, 15, 20, 40, and 60 kPa were embedded in a 5 kPa background. The ST-HMI-derived peak-to-peak displacement (P2PD) successfully detected all inclusions with R^2=0.93 of the linear regression between the P2PD ratio of background to inclusion versus Young's moduli ratio of inclusion to background. The contrasts of 10 and 15 kPa inclusions were higher in ST-HMI than ARFI-derived images. In the mouse study, the median P2PD ratio of tumor to non-cancerous tissues was 3.0, 5.1, 6.1, and 7.7 at 1, 2, 3, and 4 weeks post-injection of the tumor cells, respectively. In the clinical study, ST-HMI detected breast masses including fibroadenoma, pseudo angiomatous stromal hyperplasia, and invasive ductal carcinoma with a P2PD ratio of 1.37, 1.61, and 1.78, respectively. These results indicate that ST-HMI can assess the mechanical properties of tissues via generation and tracking of harmonic motion "on-axis" to the ARF. This study is the first step towards translating ST-HMI in clinics.**

***Index Terms*— Harmonic motion imaging; ARFI; Elasticity imaging; Breast Cancer; Ultrasound; High-Frequency ARF.**

I. INTRODUCTION

The mechanical properties of biological tissues depend on their underlying microscopic and macroscopic structures and compositions. Therefore, the changes in the mechanical properties are associated with a broad spectrum of pathologies given that diseases change the structures and compositions of the molecular building blocks of tissues. The mechanical properties of tissues can be assessed either using ultrasound elastography (UE) [1], magnetic resonance elastography (MRE) [2], or optical coherence elastography (OCE) [3]. The UE is favorable in many cases due to its low cost, ease of use, portability, real-time capability, ability to penetrate deeper in tissue, and ability to characterize the motion within the human body. Over the last three decades, different UE methods [1] for interrogating the mechanical properties have been developed and applied to diagnose diseases in liver [4], [5], breast [6], [7], thyroid [8], prostate [9], kidney [10], [11], muscles [12], [13], carotid artery [14], [15], and lymph nodes [16]. Note, mechanical properties and stiffness are used synonymously throughout the manuscript.

Among the various UE approaches are those that exploit acoustic radiation force (ARF) [17] to induce motion within the tissue. ARF based methods either use displacements "on-axis" to the ARF [18]–[21], or shear wave propagation "off-axis" to the ARF [22]–[25] or both [26], [27] to assess the mechanical properties. Both "on-axis" and "off-axis" –based methods have their pros and cons. Shear wave-based methods provide quantitative mechanical properties like elasticity and viscosity. However, shear wave-based measurements are subject to shear wave reflections and distortions artifacts in the finite and heterogeneous media. In addition, the shear wave is calculated by averaging over a 2-5 mm lateral window which leads to a reduction in spatial resolution of the mechanical properties [28]. Finally, shear wave assessments may be limited in deeper organs, obese patients, and/or stiffer tissues due to the reduction of "off-axis" displacements with shear wave propagation [29].

In contrast to the shear wave-based measurements, the "on-axis" displacement-based methods provide qualitative assessments of the mechanical properties as the force or stress is generally unknown but with added benefits. First, displacements are less distorted by heterogeneity as the displacements are observed immediately following the ARF excitation. Second, the "on-axis" method supports the finer spatial resolution of mechanical features as the mechanical properties are measured without lateral averaging [28]. Third, displacements are greatest at the on-axis to ARF and therefore, the "on-axis" method can assess the mechanical properties in deeper organs, obese patients, and/or stiffer tissues.

Some "on-axis" ARF- based methods include acoustic radiation force impulse (ARFI) imaging [18], ARF creep imaging [30], viscoelastic response (VisR) ultrasound imaging [21], [31]–[33] and harmonic motion imaging (HMI) [20]. The main difference between the HMI with other "on-axis" based methods is that an amplitude modulated (AM)-ARF (AM-ARF) is used to generate harmonic oscillations of tissue whereas other "on-axis" methods use pulsed ARF. The advantage of using

Manuscript submitted January 05, 2021; accepted January 20, 2021. This work was supported by NIH under Grant R01 CA228275 (Corresponding author: Md Murad Hossain). M. M. Hossain, N. Saharkhiz, and E. E. Konofagou are with the Department of Biomedical Engineering, Columbia University, New York, NY 10027 USA. (mh4051@columbia.edu).

This article has been accepted for publication in a future issue of this journal, but has not been fully edited. Content may change prior to final publication. Citation information: DOI 10.1109/TMI.2021.3055779, IEEE Transactions on Medical Imaging

harmonic excitation is the fact that motion at the input oscillation frequency can be easily filtered from reverberation, movement, and breathing artifacts. Previously, the HMI has been used for detecting pancreatic tumors [34], monitoring treatment response of pancreatic tumors [35], monitoring high intensity focused ultrasound-induced ablation of tumors [36], [37], and livers [38]. In the current HMI configuration, a focused ultrasound and imaging transducer simultaneously generates and tracks AM-ARF-induced motion, respectively, and a 2-D image is generated by mechanically translating both transducers. The current use of two different transducers with a mechanical positioner to generate a 2-D image renders the HMI system highly complex to use for diagnostic imaging. The data acquisition would be facilitated if the generation and tracking of harmonic motion could be performed by a single imaging transducer with electronic steering.

Towards the goal of facilitating HMI data acquisitions, this study investigates the feasibility of generating and mapping harmonic motion "on-axis" to the ARF using an imaging transducer. This new HMI method, named single transducer-HMI (ST-HMI), generates the AM-ARF by modulating the excitation pulse duration and estimates the AM-ARF-induced motion by transmitting the tracking pulses in between the excitation pulses. Note, changes in the excitation pulse duration change the integrated intensity of the pulse which in turn generates different magnitude ARF [18]. Previously, Chen *et al.* developed shearwave dispersion ultrasound vibrometry (SDUV) to generate and track harmonic shear waves using a single transducer [39]. However, a fixed duration ARF excitation pulse oscillates at a particular frequency in the SDUV which produces shear waves with comparable amplitudes of fundamental versus harmonic frequencies. The wave energy is distributed over several harmonics in the SDUV which may limit its application in a low SNR scenario. Sadeghi *et al.* developed harmonic shear wave imaging (HSWI) to generate narrowband shear waves by modulating ARF excitation pulse duration with an amplitude of the fundamental frequency several times higher than the harmonics frequencies amplitude [40]. However, the HSWI is an "off-axis" ARF-based method and the performance of HSWI was validated in the homogeneous materials only. To the best of our knowledge, there is no "on-axis" method that uses a single transducer for both generating and tracking the harmonic motion.

The objectives of this study are as follows. First, the feasibility of generating and tracking harmonic motion "on-axis" to the ARF using a single transducer is demonstrated in contrasting inclusions with different stiffnesses, and the performance of ST-HMI is compared to the ARFI [18]. Second, the impact of parameters related to the generation of harmonic oscillations in contrasting inclusions is investigated. Third, the feasibility of *in vivo* longitudinal monitoring of tumor progression in a breast cancer mouse model using ST-HMI with a high-frequency transducer is tested. Fourth, the feasibility of contrasting different human breast masses *in vivo* is demonstrated.

II. Materials and Methods

A. ST-HMI Excitation and Tracking Pulse Sequence

In ST-HMI, the tracking pulses were interleaved between sinusoidally varying excitation pulse duration (see Fig. 2). The tracking pulses were similar to a typical 2-cycle B-mode imaging pulse whereas the excitation pulses were long-duration pulses. Note, displacement linearly increases with the excitation pulse duration for a fixed acoustic pressure [40]. Therefore, sinusoidal variation in the excitation pulse duration generates sinusoidally modulated displacements. The sinusoidal variation in the excitation pulse duration was generated by sampling following continuous signal *ed(t)*:

$$ed\,(t) = t_{ARF}^{min} + \left(t_{ARF}^{max} - t_{ARF}^{min}\right) * \sin\left(2\pi \frac{f_{HMI}}{2} t\right) \quad (1)$$
$$0 \le t \ \le T_{HMI}$$

where, t is time, t_{ARF}^{min} and t_{ARF}^{max} are the minimum and maximum ARF excitation pulse duration, and f_{HMI} and T_{HMI} are the ST-HMI oscillation frequency and period, respectively. N_{ep} excitation pulses per period were selected by sampling (1) to generate discrete-time signal $ED[n]$ as follows:

$$ED[n] = ed(t) * \delta\left(t - n\left(T_{HMI} - t_{offset}\right)\right), \quad (2)$$
$$n = 1 \cdots N_{ep}$$

where δ is the delta-Dirac function and t_{offset} defines the 1st and last excitation pulse time point in a period. Equation (2) is repeated N_{cycle} times to generate a N_{cycle} cycle harmonic oscillation (see Fig. 3(b)). As the tracking pulses were interleaved between the excitation pulses, the total number of tracking pulses depends on N_{ep} and tracking pulse repetition frequency (PRF). A reference tracking pulse was transmitted first and the induced displacement was estimated with respect to the reference tracking pulse. An excitation pulse was transmitted just after reference tracking pulse if t_{offset} = 0 ms. However, the tracking pulses were collected until t_{offset} if t_{offset} > 0 ms (see Fig. 2). Note, both focused excitation and tracking beams were generated using sub-aperture depending on the F-number and focal depth. Then, both focused excitation and tracking beams were translated electronically across the lateral field to generate a 2-D image (see Fig. 3).

B. Safety Measurements Associated with ST-HMI

To evaluate the safety of ST-HMI, acoustic pressure and intensity of the excitation pulses and temperature rise during the entire ST-HMI sequence were measured. The acoustic pressure was measured by a calibrated hydrophone (Model HGL-0020, Ondo Corporation, Sunnyvale, CA, USA) mounted on a mechanical stage and controlled by stepper motors. The experiment was performed by submerging the hydrophone and L7-4 transducer (Philips Healthcare, Andover, MA, USA) in a water tank. The transducer was operated by the Verasonics research system (Vantage 256, Verasonics Inc., Kirkland, WA, USA). The oscillation frequency, excitation pulse number per cycle, focal depth, excitation pulse center frequency, and excitation voltage were fixed to 220 Hz, 8, 20 mm, 4.0 MHz, and 35 V, respectively. The derated mechanical index ($MI_{0.3}$), spatial peak temporal average ($I_{SPTA,0.3}$), and spatial peak pulsed average ($I_{SPPA,0.3}$) were calculated by derating the measured pressure at a rate of 0.3 dBcm^{-1}MHz^{-1} [24]. As the ST-HMI excitation contains several excitation pulses, the combined excitation $I_{SPTA,0.3}$ was calculated by summing the contribution of all pulses [41] as $I_{SPTA,0.3} = \sum_{i=1}^{N_{ep}} PII_{0.3}^{i} * f_{HMI}$ where $PII_{0.3}^{i}$ is the derated pulse intensity integral of the ith excitation pulse. $I_{SPPA,0.3}$ was calculated as $I_{SPPA,0.3} = \sum_{i=1}^{N_{ep}} PII_{0.3}^{i} \; / \; \sum_{i=1}^{N_{ep}} D^{i}$ where D^i is the duration of the ith excitation pulse. All the signals acquired by the hydrophone were digitized with a Tetronix oscilloscope (Tektronix, Inc, Beaverton, Oregon, USA).

Temperature rise due to the entire ST-HMI sequence (i.e., all RF-lines) was measured by introducing a needle-type thermocouple (Thermo Works T-29X, UT, USA) between the transducer and a piece of the canine liver which were submerged in 37^{o}C water. The thermocouple was posited laterally at the center of the field of view (FOV) and axially, first at 1 mm and then, 20 mm from the transducer surface to measure the temperature rise at transducer surface and focal depth, respectively. Two repeated measurements were taken at each position and the average of the two measurements was calculated.

C. Phantom Experiments

Imaging of two commercially available elastic phantoms (customized model 049A, CIRS, Norfolk, VA, USA) was performed using a Verasonics research system with an L7-4 transducer. The transducer was held in a steady position using a clamp during imaging. In both phantoms, three stepped-cylindrical inclusions with varying diameters were embedded in a 5 ± 1.0 kPa background. The manufacturer-provided Young’s moduli of 6 inclusions were 8 ± 1.5, 10 ± 2, 15 ± 3, 20 ± 4, 40 ± 8, and 60 ± 10 kPa. The imaging was performed at 10 ± 1.0 mm diameter cross-section of the cylindrical inclusions. The center of the inclusion was approximately 15 mm from the phantom’s surface. Throughout the remainder of the manuscript, each inclusion will be represented by its mean nominal Young’s modulus value.

First, the performance of ST-HMI was compared to ARFI [18] by imaging 5 kPa homogenous region in the background and 8, 10, and 15 kPa inclusions. The ARFI imaging was performed using the methods described in [18], [42]–[44] with parameters indicated in Table I. In all inclusions, ST-HMI was performed using f_{HMI} = 220 Hz, N_{ep} = 8, t_{offset} = 0.2 ms, and N_{cycle} = 5 with parameters indicated in Table I. For two-dimensional ST-HMI and ARFI imaging, 34 evenly spaced RF-lines with 0.6 mm spacing between RF-lines were acquired for the respective imaging modality. The size of the excitation beam in the lateral direction was 0.86 mm. There was also a 0.1 s interval between RF-lines for electronic switching between sub-apertures and charging the power supply which is enough for tissue recovery from the micron-level displacements. Thus, there will be no interference in the tissue mechanical response due to the overlapping excitation size of RF-lines. To reduce transducer face heating, the entire HMI-data were collected using wiper blading scanning mode [11]. In this scanning mode,

Table I

EXCITATION AND TRACKING PARAMETERS OF ACOUSTIC RADIATION FORCE IMPULSE (ARFI) USED IN IMAGING PHANTOMS AND SINGLE TRANSDUCER-HARMONIC MOTION IMAGING (ST-HMI) USED IN IMAGING PHANTOMS, *IN VIVO* BREAST CANCER PATIENTS, AND BREAST CANCER MICE WITH NORMALIZED CROSS CORRELATION PARAMETERS FOR DISPLACEMENT ESTIMATION. METHOD (ARFI/ST-HMI) IS NOT INDICATED FOR COMMON PARAMETERS. PH. = PHANTOM

Parameters	Phantom /Human	Mouse
Beam sequence parameters of ST-HMI / ARFI		
Transducer	L7-4	L22-14vXLF
Bandwidth	58%	51%
Sampling frequency	20.84 MHz	62.5 MHz
Acoustic lens axial focus	25 mm	20 mm
Excitation pulse frequency	4.0 MHz	15.6 MHz
Excitation pulse F-number	2.25	2.25
Tracking pulse frequency	6.1 MHz	20.8 MHz
Tracking pulse transmit F-number	1.75	1.75
Tracking pulse receive F-number *	1.0	1.0
Excitation and tracking pulse axial focus	15 mm (pha.) 14 ± 3.6 mm (Human)	11.3 ± 0.5 mm
Minimum excitation pulse duration (t_{ARF}^{min}, ST-HMI)	28 µs	20 µs
Maximum excitation pulse duration (t_{ARF}^{max}, ST-HMI)	55 µs	30 µs
Oscillation frequency (ST-HMI)	60-420 Hz (phantom) 220 Hz (Human)	200 Hz
Oscillation cycle number (ST-HMI)	2-10	5
Single excitation pulse duration (ARFI)	87.5 µs	-
Tracking pulse number (ARFI)	110	-
Tracking pulse PRF	10 KHz	10 KHz
Spacing between RF-lines	0.59 mm	0.3 mm
RF-lines number per 2-D image	34	14
Lateral field of view size	20 mm	4.2 mm
Normalized cross correlation parameter		
Interpolation factor	4	4
Kernel length	592 µm	295 µm
Search region	80 µm	80 µm

* Aperture growth and dynamic Rx focusing enabled

RF-lines were acquired in a non-serial order across the lateral FOV. First, a single RF-line was captured from the far left of the FOV, then in the middle of the FOV, then one position to the right of the far left, then one position to the right of the middle, and so on, such that no two consecutive RF-lines were captured in two adjacent lateral locations. Therefore, this scanning mode will also prevent interference in the tissue mechanical response between consecutive RF-lines. Preceding each 2-D ST-HMI acquisition was one spatially-matched B-mode image, with 128 lateral lines spanning approximately 38 mm. Besides evaluating the performance of ST-HMI in contrasting different stiffness inclusions and comparing the performance with ARFI, the impact of f_{HMI}, N_{ep}, t_{offset}, and N_{cycle} on the ST-HMI images was evaluated by imaging 15 ± 3 kPa and 60 ± 10 kPa inclusions. The impact of oscillation frequency was investigated by varying f_{HMI} from 60 Hz to 420 Hz in steps of 40 Hz. The number of excitation pulses per cycle was varied between oscillation frequencies to keep the I_{SPTA} (i.e., the duty cycle of HMI excitation) constant. The duty cycle of excitation was calculated as $100 * \sum_{i=1}^{N_{ep}} D^i \; / \; T_{HMI}$. The excitation duty cycle was kept around 8% by using N_{ep} of 30, 18, 13, 10, 8, 7, 6, 5, 5, and 4 for f_{HMI} of 60, 100, 140, 180, 220, 260, 300, 340, 380, and 420 Hz, respectively. N_{cycle} and t_{offset} were fixed to 5 and 0.2 ms, respectively for all oscillation frequencies.

To investigate the effect of duty cycle on ST-HMI's performance, the same two inclusions were imaged with variable (duty cycle, N_{ep}) of (3.8%, 5), (6.36%, 8), (8.88%, 11), and (11.36%, 14), but with fixed f_{HMI} =180 Hz, t_{offset} = 0.2 ms and N_{cycle} = 5. The impact of the oscillation cycle number was investigated by varying N_{cycle} from 2 to 10 in steps of 2 with fixed f_{HMI} = 420 Hz, N_{ep} = 4, and t_{offset} = 0.2 ms. Finally, the t_{offset} was varied from 0 to 0.6 ms in steps of 0.2 ms with fixed f_{HMI} = 180 Hz, N_{ep} = 10 and N_{cycle} = 5. There was a slight change in the duty cycle (7.4-8.5%) due to the change in the t_{offset}.

For each case, six repeated acquisitions were performed by moving the transducer in the elevational direction. The acquisition time of ST-HMI data with 34 RF-lines took approximately 5-7s with 0.1s interval between RF-lines. Therefore, the frame rate was approximately 0.15- 0.2 Hz.

D. Imaging of A breast cancer mouse model, In Vivo

The orthotropic, 4T1 breast cancer mouse model (N=4) was used to investigate the performance of ST-HMI in monitoring longitudinal changes in tumor stiffness. The induction of cancer and imaging protocols were reviewed and approved by the Columbia University Irving Medical Center (CUIMC) Institutional Animal Care and Use Committee (IACUC). Eight to ten-week-old female BALB/c mice were purchased from the Jackson Laboratory. Cancer was inducted by injecting 2 x 10^5 4T1 breast cancer cells in the 4^{th} inguinal mammary fat pad [45], [46].

ST-HMI of the anesthetized mice (1- 2% isoflurane in oxygen) was performed using the same Verasonics research system with L22-14vXLF (Vermon, Tours, France) linear array. Imaging was performed by placing the mice in a supine position on a heating pad with their abdominal hair removed. The transducer was held in a steady position using a clamp and was placed in a container filled with degassed water and an acoustically transparent membrane at the center.

Mice were imaged at 1, 2, 3, and 4 weeks post-injection of tumor cell using the parameters indicated in Table I with f_{HMI} = 200 Hz, N_{ep} = 13, t_{offset} = 0.7 ms, and N_{cycle}= 5. A 2-D HMI image was formed by acquiring fourteen evenly spaced RF-lines with 0.3 mm separation which resulted in approximately 4.2 mm lateral FOV in the ST-HMI images Note, the lateral size of the excitation beam was 0.22 mm for the L22-14vXLF transducer. One spatially-matched B-mode image was acquired with 128 lateral lines spanning approximately 13.6 mm, for anatomical reference. If the tumor size was larger than the ST-HMI lateral FOV, multiple acquisitions were acquired by mechanically translating the transducer in lateral directing using a 3-D positioning system (Velmex Inc., Bloomfield, NY, USA). The final image was reconstructed from all the acquisitions.

E. Imaging of Patients with Breast Masses, In Vivo

The clinical performance of ST-HMI was evaluated by imaging female patients with breast masses (N=3) following human subjects protocol approval by the CUIMC Institutional Review Board (IRB). Informed consent was obtained from all enrolled subjects. Two patients with suspicious breast masses were scheduled to undergo needle biopsy and one patient diagnosed with invasive ductal carcinoma (IDC) was scheduled for the breast segmentectomy. Similar to the phantom experiments, ST-HMI was performed using the same Verasonics research system with an L7-4 linear array with parameters indicated in Table I. Patients were imaged in a supine or lateral oblique position. The location and boundaries of the tumors were confirmed by an experienced sonographer in the B-mode ultrasound image. The transducer was hand-held during imaging. Data were collected by orienting the transducer parallel to the radial direction (i.e., line connecting center of mass and nipple).

F. ST-HMI and ARFI Data Processing

For all the ST-HMI and ARFI acquisitions, channel data were transferred to the computational workstation for offline processing using MATLAB (MathWorks Inc., Natick, MA, USA). A custom delay-and-sum beamforming [47] was applied to construct beamformed radiofrequency (RF) data. Motion tracking with respect to the reference tracking pulse was performed using 1-D normalized cross-correlation (NCC) [48] with parameters as indicated in Table I. After motion tracking, a 3-D dataset (axial x lateral x time) describing axial displacements over time was generated.

To generate a 2-D parametric image in ARFI [42], [43], a linear filter [49] was applied to the displacement versus time profile at each axial x lateral pixel to reduce motion artifacts. Then, the peak displacement (PD) over time was calculated from each filtered displacement profile and rendered into a 2-D parametric image. ARFI-derived PD images were normalized to account for the variation in the ARF magnitude over the axial range [50]. The normalized PD image was compared to the ST-HMI image.

To generate a 2-D parametric image in ST-HMI, the differential displacements at each lateral x axial pixel were computed by subtracting displacements between successive time points to remove the slowing varying motion. Then, the desired oscillation of f_{HMI} Hz was filtered out using a second-order Butterworth bandpass filter (*butter* and *filter* function).

The cutoff values of the bandpass filter were selected adaptively for each data acquisition. The cutoff values were calculated by finding the 1st minima around f_{HMI} in fast Fourier transform (FFT) (see green circle in Fig. 4 (c)). The minimum FFT magnitude around f_{HMI} was found by calculating the successive difference in magnitude and then, finding the change in sign (*sign* function) in the differential magnitude. As an example, the sign of differential magnitude was changed from negative to positive and positive to negative for lower and higher cutoff values. The adaptive cutoff values were calculated at (axial, lateral) location of ([focal depth and focal depth ± 5 mm], [-9.5, -4.5, 0.5, 5.5, and 9.5 mm]) and ([focal depth], [-2.0, -1.0, 0.0, 1.0, and 2.0 mm]) for L7-4 and L22-14vXLF transducers, respectively instead of all pixels to expedite the data processing. Then, the final lowest and highest cutoff values for filtering all pixels were the medians of lower and higher cutoff values derived at the selected locations. The filtered displacement profile at each pixel was integrated (*cumsum* function in MATLAB) and normalized to a zero mean (i.e., the mean was subtracted from the integrated-filtered displacement profile). Using the integrated-filtered displacement profile, the average peak-to-peak displacement (P2PD) over N_{cycle} cycles was calculated at each axial x lateral pixel, and then, rendered into a 2-D parametric image (see Fig. 5(b)).

The P2PD is a function of the ARF amplitude which varies over the axial range. Therefore, the depth-dependent variation in P2PD must be normalized before the P2PD can be compared over the axial range. The normalizing term $\overline{P2PD(x)}$ was derived as the median *P2PD(x)* over a lateral range in a reference region which is a presumed mechanically homogeneous region. Therefore, the median P2PD over a lateral range was computed for each axial location (x). Then, the final normalized 2-D P2PD image was constructed by dividing each lateral line by the normalizing term $\overline{P2PD(x)}$. Therefore, the final normalized P2PD image represented the stiffness with respect to the stiffness of the reference region i.e., if a pixel with a normalized P2PD value of 2 means the pixel is 2 times softer than the pixel at the corresponding depth in the reference regions. A similar normalization technique was performed for ARFI [50] and VisR images [31]. Fig. 1 depicts a flow chart representing the processing steps implemented to generate normalized P2PD images in the ST-HMI imaging.

The acquired ST-HMI data were processed offline in a 2.2 GHz Intel Xeon platinum processor using 16 cores parallel processor. Depending on the oscillation frequency, it took 3-4 min to process data from performing the delay-and-sum beamforming to generating the final normalized P2PD image. Note, higher oscillation frequencies have a shorter period and take a shorter time to process the data. The computational time can be reduced by implementing ST-HMI data processing pipelines (Fig. 1) in CUDA GPU.

G. Image Quality Metrics

Contrast and contrast-to-noise ratio (CNR) of ST-HMI and

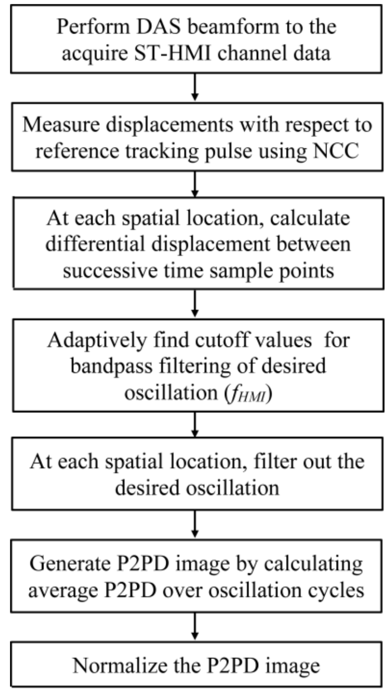

Fig 1: Data processing steps employed to generate ST-HMI-derived peak-2-peak displacement (P2PD) image. DAS = Dealy-and-sum; NCC = Normalized cross-correlation;

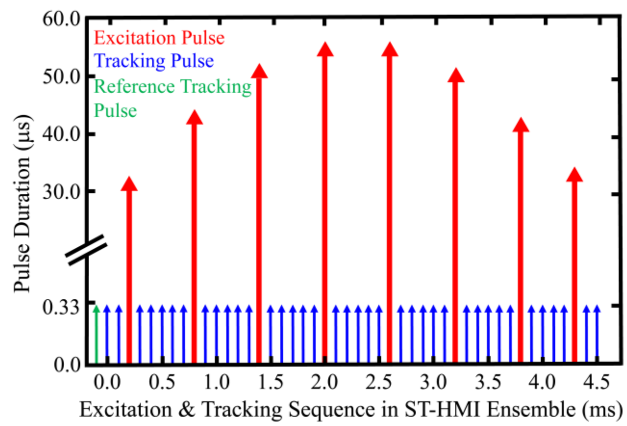

Fig 2: ST-HMI pulse sequence with the duration of excitation (red) and tracking (blue and green) pulse for 220-Hz oscillation frequency, 0.2 ms offset, and 8 excitation pulses per cycle. Y-axis contains a break to accommodate the difference in excitation and tracking pulse duration. The duration of excitation pulses is variable to generate amplitude-modulated force whereas the duration of tracking pulses is fixed. Displacement was estimated with respect to the reference tracking pulse (green).

ARFI-derived inclusions' images were calculated for the quantitative comparison. For contrast and CNR calculations, the inclusion's region of interest (ROI) was defined as the concentric circle with 80% of the corresponding inclusion's radius. The background ROI was defined as a ring surrounding the inclusion, with an inner radius of 120% of the corresponding inclusion' radius. The outer radius was varied between the inclusions depending on their size so that the inclusion's and background's ROI had equal areas (see Fig. 7). Contrast and CNR were calculated as $|\mu_{INC} - \mu_{BKD}| / \mu_{BKD}$ and

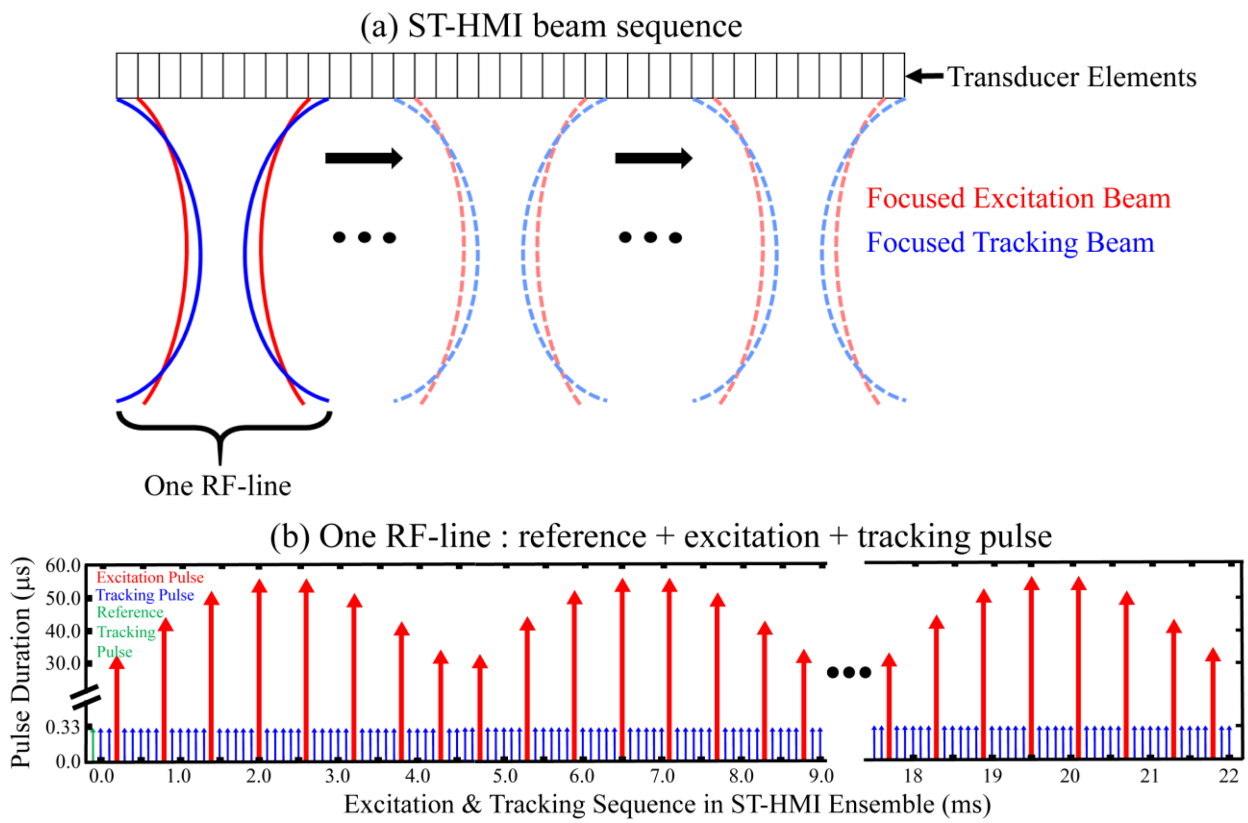

Fig 3: (a) Focused excitation and tracking beams electronically translated across lateral field to generate a 2-D image in ST-HMI. (b) One RF-line consists of reference, excitation, and tracking pulses with several cycles of 220 Hz oscillation.

$|\mu_{INC} - \mu_{BKD}| \; / \; \sqrt{(\sigma_{INC}^2 + \sigma_{BKD}^2)}$, respectively, where, μ and σ are the median and standard deviation of normalized displacements in the inclusion's (INC) and background's (BKD) ROI. To compare the P2PD ratio of background to inclusion with Young's moduli ratio of inclusion to background, a rectangular ROI (see Fig. 7) was used to avoid the boundary effects. The inclusion's ROI was defined as a rectangle with a height and width of 40% of the inclusion's radius. The background's ROI was defined as the two rectangles positioned 3.5 mm from the inclusion's boundary, each with a height equal to the inclusion's ROI height and width equal to half of the inclusion's ROI width. The inclusion's boundary was derived from the B-mode image (see Fig. 5a).

H. Statistical Analysis

All statistical analyses were carried out using MATLAB. Nine separate two-sample Wilcoxon signed rank-sum tests (*signrank* function) were carried out to compare ARFI versus ST-HMI-derived contrast, CNR, and displacement ratio of 8, 10, and 15 kPa inclusions. Ten separate Kruskal-Wallis tests (*kruskalwallis* function), were carried out to compare the contrast and CNR of ST-HMI derived images across different inclusions, across oscillation frequencies, across excitation pulse duty cycles, across oscillation cycle numbers, and across excitation pulse offsets. If any group was statistically significant, two-sample Wilcoxon signed rank-sum tests were used to find which combination was statistically significant. The R^2 of the linear regression between the P2PD ratio and Young's moduli ratio was calculated. Two separate Kruskal-Wallis tests were carried out to compare tumor diameters and P2PD ratios across imaging time points. Two-sample Wilcoxon rank-sum tests (*ranksum* function) were used to find which combination was statistically significant. For all the analyses, the statistical significance was based on a two-sided α of 0.05.

III. Results

Fig. 2 shows excitation (red) and tracking (blue and green) pulse sequence for one-period oscillation with f_{HMI} = 220 Hz, N_{ep} = 8, and t_{offset} = 0.2 ms. The duration of excitation pulses was varied to generate AM-ARF whereas the tracking pulse duration was fixed. This pulse sequence was repeated to generate 5 cycles of oscillation at each RF line. The $MI_{0.3}$, $I_{SPTA,0.3}$, and $I_{SPPA,0.3}$ associated with the sequence were 1.37, 10.5 Wcm^{-2}, and 194.38 Wcm^{-2}, respectively. The mean temperature rise due to the entire beam sequence was 0.4°C and 0.6°C at the focal depth (20 mm) and the surface of the transducer, respectively.

Fig 3 shows the excitation and tracking beams sequence to generate a 2-D image in ST-HMI. Focused excitation and tracking beams were electronically translated across the lateral field to generate a 2-D image (panel (a)). The number of elements in the sub-aperture to generates excitation and tracking beams depends on the F-number and focal depth. Panel (b) shows that one RF-line with several cycles of 220 Hz oscillation at each lateral location was generated by transmitting reference, excitation, and tracking pulses.

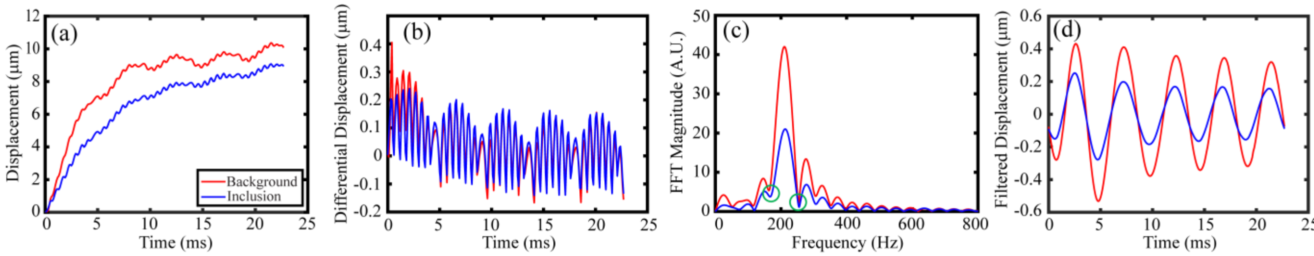

Fig. 4: ST-HMI derived (a) displacement profiles (b) differential displacement between successive time points (c) magnitude spectrum of fast Fourier transform (FFT) of the differential displacement profiles (d) filtered displacement profiles in 15 kPa inclusion (blue) and 5 kPa background (red). Green circles represent cutoff values for the bandpass filter. ST-HMI oscillation frequency was 220 Hz with 0.2 ms offset and 8 excitation pulses per cycle.

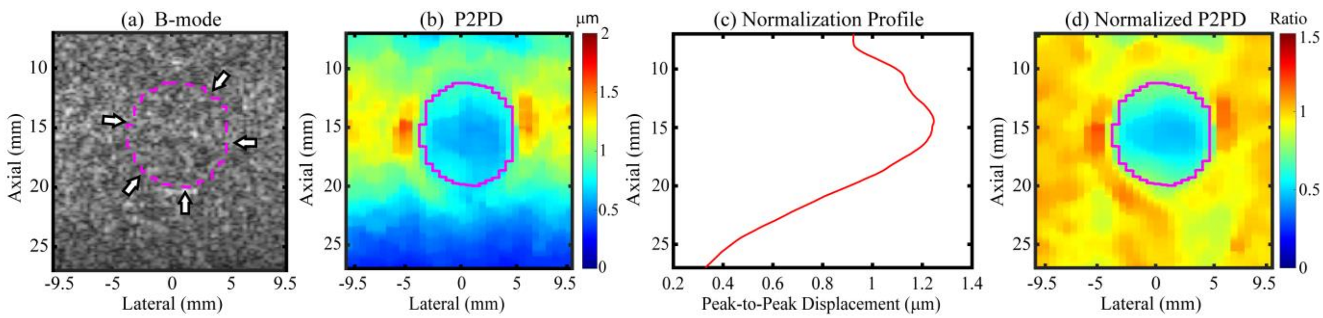

Fig 5: (a) Bmode ultrasound image and (b) ST-HMI derived peak-to-peak displacement (P2PD) image of a 15 kPa inclusion embedded in a 5 kPa background. (c) Axial distance versus median P2PD over a lateral distance of [-10 -8.2] and [7.9 9.7] mm. (d) Normalized P2PD of the same inclusion. Magenta contour represents the inclusion boundary derived from the B-mode ultrasound image. Arrowhead in the B-mode image indicates slightly hypoechoic regions in the inclusion's boundary.

Fig. 4(a) shows two representative displacement profiles as a function of time in 5 kPa background (red) and 15 kPa inclusion (blue), respectively. The differential displacements of the same two profiles are shown in panel (b). The envelope of differential displacements clearly underwent a 220-Hz oscillation which was confirmed by the peak at 220 Hz in the FFT of differential displacement profiles (panel (c)). The filtered displacement, shown in panel (d), contained only 220-Hz oscillation. The average P2PDs from the filtered profiles were 0.74 and 0.38 μm for the background and inclusion, respectively.

A 2-D image was generated by calculating P2PD at each pixel (Fig. 5(b)). However, the P2PD varied over the axial range due to the variation in ARF amplitude over depth (panel (b) and (c)). The depth normalization profile (panel (c)) was calculated from the background to generate the normalized P2PD image (panel (d)). The normalization profile was generated by averaging P2PD over a lateral distance of [-10 -8.2] and [7.9 9.7] mm.

Fig. 6 qualitatively compares the ST-HMI and ARFI-derived images of a homogeneous region in a 5 kPa background and 8, 10, and 15 kPa inclusions embedded in a 5 kPa background. Qualitatively, ST-HMI-derived normalized P2PD and ARFI-derived normalized PD images look very similar except for 15 kPa inclusions. The (mean, standard deviation) of ST-HMI-derived normalized P2PD and ARFI-derived normalized PD of the homogeneous background was (1.008, 0.049) and (1.008, 0.047), respectively. The coefficient of variation (CoV = 100* standard deviation/mean) of P2PD and PD was 4.86% and 4.66%, respectively which indicate images were homogeneous. The contrast and CNR of (ST-HMI, ARFI)-derived images were (0.23, 0.24) and (2.1, 2.1) for 8 kPa, (0.38, 0.31) and (3.2, 3.3) for 10 kPa, and (0.46, 0.40) and (4.2, 4.3) for 15 kPa inclusion, respectively.

Fig. 7 qualitatively compares the normalized P2PD images of 8, 10, 15, 20, 40, and 60 kPa inclusions embedded in a 5 kPa background. Note, the ST-HMI images of 8, 10, and 15 kPa inclusions were at a slightly different elevational plane in Figs. 6 versus 7. The inclusion's contrast increased with the inclusion's Young's modulus, which is also evident in Fig. 8. Fig. 8(a) shows that the contrast and CNR of both ARFI and ST-HMI-derived images increased with Young's moduli ratio of inclusion to background. The contrast was not statistically different between ARFI versus ST-HMI images of 8 kPa inclusion but was statistically different between ST-HMI versus ARFI images of 10 and 15 kPa inclusions. The CNR was not statistically different between ARFI versus ST-HMI images of any of the three inclusions images. The ST-HMI-derived P2PD ratios of background to inclusion were highly correlated with Young's moduli ratios of inclusion to background (panel (b)) with R^2=0.93. The ARFI-derived PD ratio was not statistically different from the ST-HMI-derived P2PD ratio in the 8 kPa inclusion but was statistically different for 10 and 15 kPa inclusions. Note, all inclusions were imaged with f_{HMI} = 220 Hz.

Fig. 9 qualitatively demonstrates the impact of the oscillation frequency in contrasting 15 and 60 kPa inclusions. Two observations are notable. First, the perceived size of the inclusion in the ST-HMI image became similar to the true size with higher frequencies in both phantoms. Second, lower frequencies (60, 100, and 180 Hz) distorted the size of the stiffer inclusion more (60 kPa versus 15 kPa).

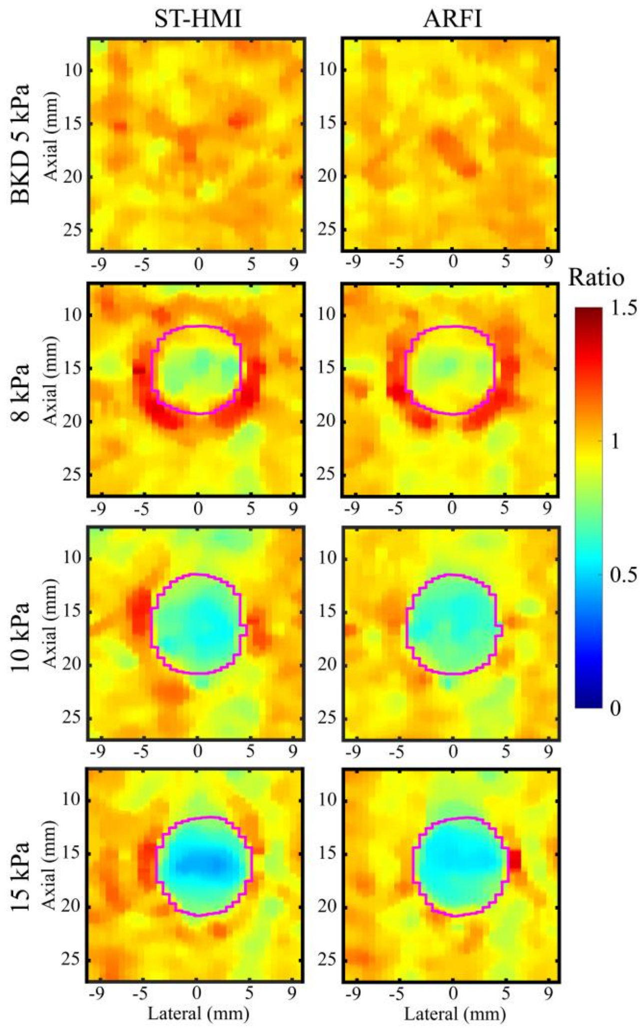

Fig 6: ST-HMI derived normalized peak-to-peak displacement (left column) and ARFI-derived normalized peak displacement (right column) images of homogenous background (BKD, 1st row) and 8 kPa (2nd row), 10 kPa (3rd row) and 15 kPa (4th row) inclusions. Magenta contour represents the inclusion boundary derived from the B-mode ultrasound image.

Fig. 10 demonstrates that the contrast and CNR of 15 and 60 kPa inclusions increased with frequencies until 140 and 220 Hz, respectively, and then, reached a plateau. The Kruskal–Wallis test suggested that contrast and CNR were statistically different across frequencies for both inclusions. The highest median (contrast, CNR) occurred at (180, 300) Hz and (180, 260) Hz for 15 and 60 kPa inclusions, respectively. The signed ranksum test rules that the contrast at 180 Hz was statistically different from all other frequencies for both inclusions. The CNRs at 300 and 260 Hz were statistically different from all the frequencies except 260 Hz and the frequencies less than 220 Hz for 15 and 60 kPa inclusions, respectively.

Fig. 11 shows the effect of the excitation duty cycle (left column), oscillation cycle number (center column), and excitation pulse offset (right column) on the contrast (top row) and CNR (bottom row) of 15 and 60-kPa inclusions. Four observations are notable. First, the highest median contrast and CNR were achieved for duty cycle, cycle number, and offset of (6.36, 11.36) %, (2, 2), (0.4, 0.4) ms, and (8.88, 11.36) %, (10, 10), (0.4, 0.6) ms for (15, 60) kPa inclusions respectively. Second, the contrast and CNR did not change significantly after the duty cycle of 3.82% and 6.36 % for 60 and 15 kPa inclusion, respectively. Third, the contrast was generally higher for the lower oscillation cycle number, but CNR was higher for higher cycle numbers. Fourth, the CNR was not impacted by the change in offset and contrast did not change for offsets greater than 0 ms for both phantoms. The lowest contrast was achieved at $t_{offset} = 0$ ms which also had the lowest duty cycle.

Fig. 12 shows the normalized P2PD images of a representative mouse tumor at 1, 2, 3, and 4 weeks post-injection of the tumor cell. The depth-dependent profiles were generated from the leftmost 2 mm lateral FOV in the non-cancerous tissue (i.e., background). Two observations are notable. First, the tumor grew over time. Second, the P2PD at the tumor with respect to the non-cancerous tissues decreased over time. These observations are quantitatively demonstrated in Fig. 13, which shows that tumor diameters and the P2PD ratios of non-cancerous tissues to tumor increased over time. The median P2PD was 3.0, 5.1, 6.1, and 7.7 at 1, 2, 3, and 4 weeks, respectively. The P2PD ratio was calculated using the ROI shown in Fig. 12.

Fig. 14 shows the normalized P2PD image overlaid on the B-mode ultrasound image of human breast masses with fibroadenoma (23 yr., FA), pseudo angiomatous stromal hyperplasia (65 yr., PASH), and invasive ductal carcinoma (54 yr., IDC). The median P2PD ratio of non-cancerous tissues to tumor was 1.37, 1.61, and 1.78 in patients with FA, PASH, and IDC, respectively. The ST-HMI was able to detect as small as a 4 mm tumor (IDC).

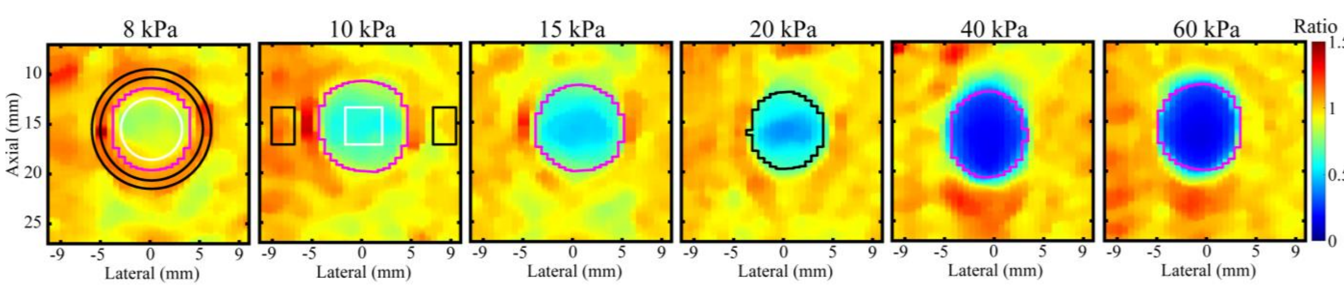

Fig 7: (a) ST-HMI derived normalized peak-to-peak displacement (P2PD) images of 8, 10, 14, 15, 20, 40, and 60 kPa inclusions embedded in a 5-kPa background of two commercial phantoms. Magenta contour represents the inclusion boundary derived from the B-mode ultrasound image. Circular and rectangular contours in the background (black) and inclusion (white) represent the region of interest for the calculation of image quality metrics and the comparison of the P2PD ratio versus the Young's moduli ratio, respectively.

This article has been accepted for publication in a future issue of this journal, but has not been fully edited. Content may change prior to final publication. Citation information: DOI 10.1109/TMI.2021.3055779, IEEE Transactions on Medical Imaging

IV. Discussion

A novel method, named ST-HMI, to assess the mechanical properties of tissue "on-axis" to the ARF was presented herein. This novel method uses a single transducer to both generate and track harmonic oscillations at the ARF-region of excitation (ROE) by interleaving the tracking pulses in between the excitation pulses. The harmonic oscillation was generated by modulating the excitation pulse duration and the P2PD was calculated after filtering out oscillation frequency (i.e., fundamental frequency). The name harmonic oscillation might be confusing from the signal processing perspective because harmonic frequency means integer multiple of the fundamental frequency in signal processing. However, in mechanics, harmonic motion usually means when the material oscillates around its original location due to a sinusoidally varying force at a specific frequency. The harmonic motion has been used to describe single fundamental frequency oscillation in the magnetic resonance elastography [51], [52] and ultrasound elastography [20], [53], [54].

The obvious advantage of ST-HMI over conventional HMI is its simplicity compared to the two-transducers and mechanical 3-D positioner based set-up of the conventional HMI. ST-HMI uses discrete excitation pulses whereas the conventional HMI uses continuous excitation pulses and monitors tissue deformation during the excitation pulse. The tissue mechanical response timing and overall type will be fundamentally different for continuous versus discontinuous excitation pulses. Future studies will rigorously compare the mechanical response of continuous versus discrete excitation pulses and how it impacts inclusion's CNR and contrast.

In addition to the HMI, the mechanical response of tissue is also different in ST-HMI versus ARFI. An excitation pulse with a fixed duration is used to generate force in ARFI and the motion is tracked after the cessation of the force [18]. Therefore, the energy of the ARFI-induced motion is spread over the broadband frequency range (0-2000 Hz). However, the energy of the ST-HMI-induced motion is contained predominantly in the modulating frequency (Fig. 4c). Despite these differences, there was no statistical difference in CNR between ST-HMI versus ARFI-derived images (Fig. 8a). However, the contrast was higher in ST-HMI versus ARFI-derived inclusions' image (Fig.8a). Despite the contrast of ST-HMI images being higher, no difference in CNR may be due to the higher standard deviation of the P2PD values in the homogenous region (Fig. 6). Higher standard deviation may be due to the local inhomogeneity in the background and inclusion materials or may be inherent in the ST-HMI data processing due to the estimation of motion at a particular frequency. However, one advantage of ST-HMI is that oscillation frequency can be optimized to improve the inclusions' CNR and contrast (Fig. 10). Note, the ST-HMI with an oscillation frequency of 220 Hz was compared with the ARFI. Future studies will rigorously compare ARFI versus ST-HMI with optimized oscillation frequency in different stiffness and size inclusions.

Another potential advantage of ST-HMI over ARFI [18] is that the ST-HMI is robust against different kinds of motion artifacts because the motion at the input oscillation frequency can be easily filtered from reverberation, movement, and breathing artifacts. However, different kinds of motion filters have been developed to remove the motion artifacts from the ARFI images [49], [55]. To rigorously compare the performance of ST-HMI versus ARFI with motion filters with and without the presence of motion artifacts is the topic of future studies.

Similar to HMI and ARFI, ST-HMI is also different from the "off-axis" shear wave-based methods like supersonic shear imaging [25], shear wave imaging [23], SDUV [39], or HSWI

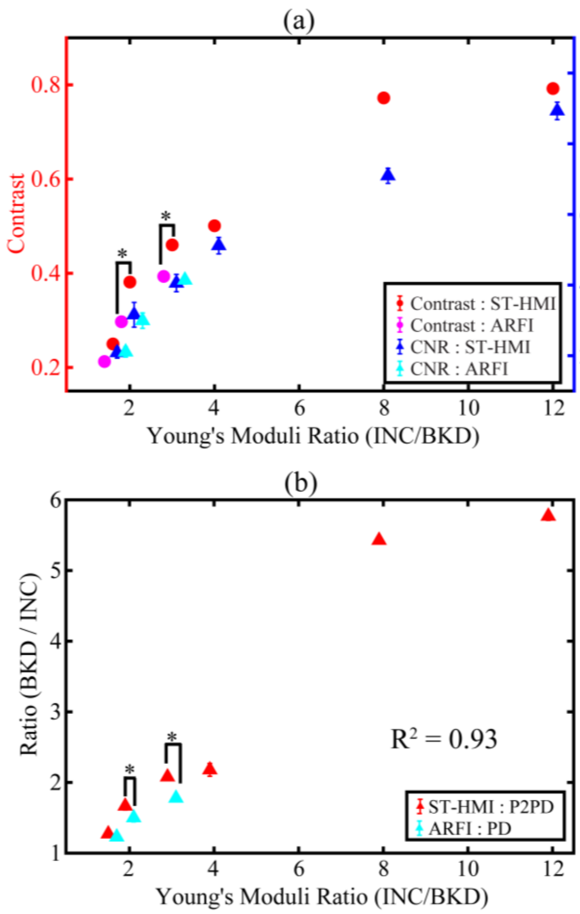

Fig. 8: (a) Contrast (red/magenta, left y-axis) and CNR (blue/cyan, right y-axis) of ARFI and ST-HMI-derived images versus Young's moduli ratio of inclusion (INC) to background (BKD). The ARFI imaging was performed only on 8, 10, and 15 kPa inclusions. The contrast was not statistically different between ARFI verus ST-HMI images of 8 kPa inclusion but was statistically different between ARFI verus ST-HMI images of 10 and 15 kPa inclusions (signed ranksum, $p<0.05$). The CNR was not statistically different between ARFI verus ST-HMI images of any of the three inclusions. All combinations of CNR and contrast of the ST-HMI images were statistically significant (signed ranksum, $p<0.05$). (b) ST-HMI-derived Peak-to-peak displacement (P2PD) and ARFI-derived peak displacment (PD) ratio of background to inclusion versus Young's moduli ratio of inclusion to background with R^2 value. The numerator and denominator are interchanged in the abscissa and ordinate's ratio as the Young's modulus and P2PD/PD are inversely related. Data are plotted as median ± 0.5* interquartile range over 6 repeated acquisitions.

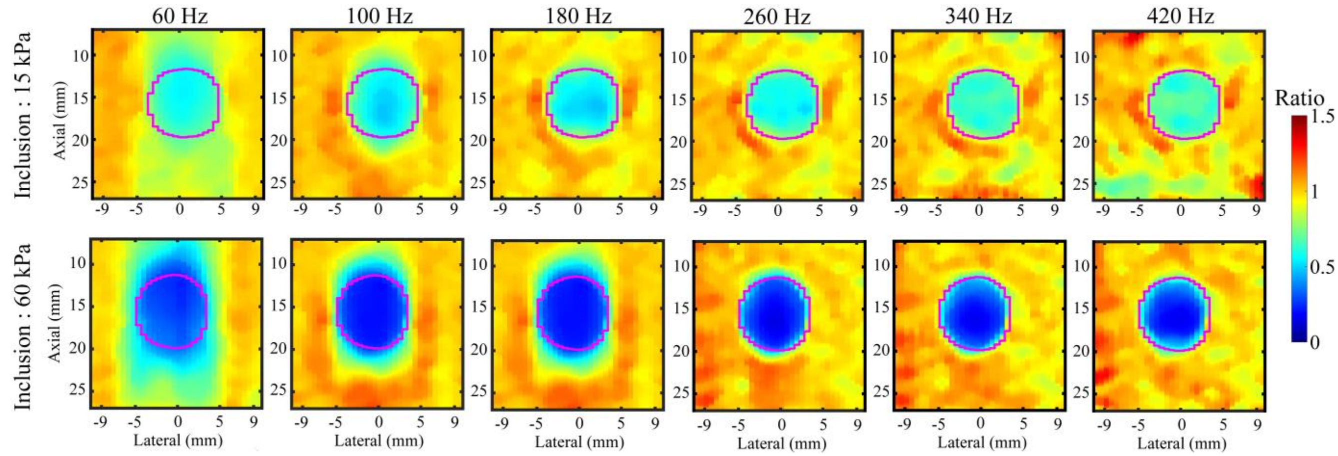

Fig 9: ST-HMI derived normalized peak-to-peak displacement images of 15 kPa (top row) and 60 kPa (bottom row) inclusions embedded in a 5 kPa background for oscillation frequency of 60 Hz (1st column), 100 Hz (2nd column),180 Hz (3rd column), 260 Hz (4th column), 300 Hz (5th column), and 420 Hz (6th column). Magenta contour represents the inclusion boundary derived from the B-mode ultrasound image.

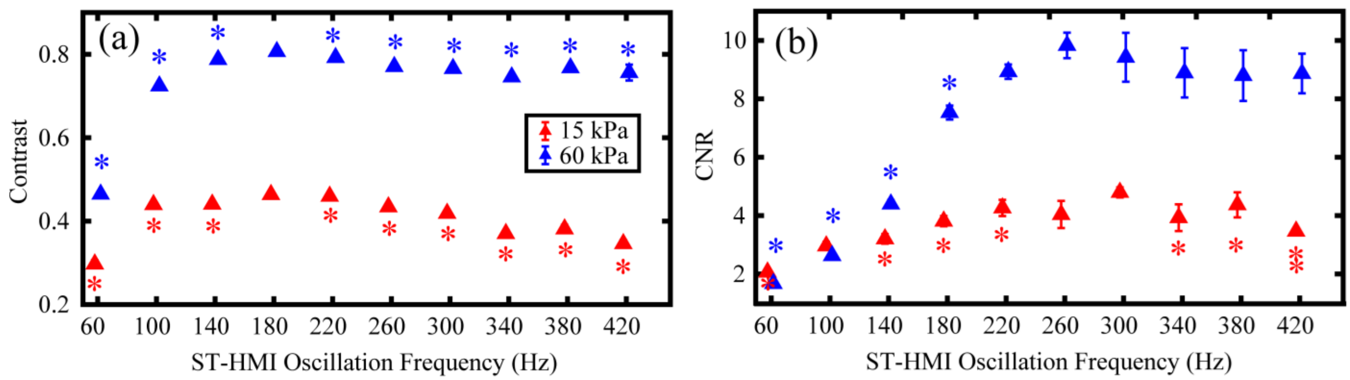

Fig 10: (a) Contrast and (b) CNR of the ST-HMI derived peak-to-peak displacement images of 15 kPa (blue) and 60 kPa (red) inclusions as a function of oscillation frequency. Data are plotted as median ± 0.5*interquartile range over 6 repeated acquisitions. The Kruskal–Wallis test suggested that contrast and CNR were statistically different across frequencies for both inclusions. For clarity, median contrast and CNR at frequencies that were statistically different (sign ranksum) from the highest median contrast (180 Hz for both inclusions) and CNR (300 and 260 Hz for 15 and 60 kPa inclusions) are shown. Blue and red asterisk (*) represent statistical significance for 15 and 60 kPa inclusions, respectively.

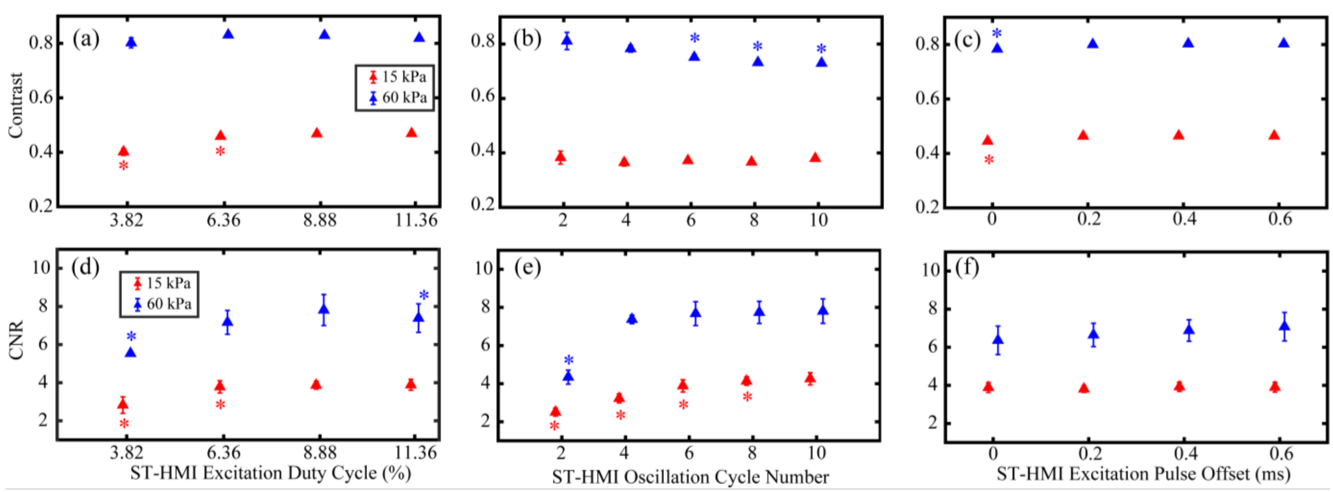

Fig. 11: Contrast (top row) and CNR (bottom row) of the ST-HMI derived peak-to-peak displacement images of 15 kPa (blue) and 60 kPa (red) inclusions versus HMI excitation duty cycle (left column), oscillation cycle number (center column), and excitation pulse offset (right column). Data are plotted as median ± 0.5*interquartile range over 6 repeated acquisitions. For clarity, the asterisk is only shown when Kruskal–Wallis test suggests a statistical difference and median contrast and CNR were statistically different from the highest median contrast and CNR.

1

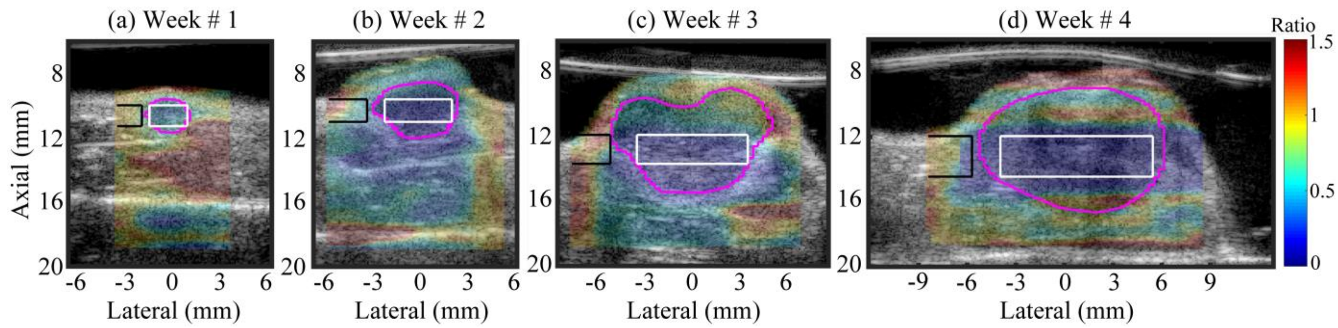

Fig 12: The normalized peak-to-peak displacement image overlaid on the B-mode ultrasound image of an orthotropic, 4T1 mouse tumor at 1, 2, 3, and 4-weeks post-injection of cancer cells. Magenta, black and white contours represent tumor boundary, the region of interest (ROI) in the non-cancerous tissues, and ROI in the tumor, respectively.

[40] in terms of estimating the mechanical properties of tissues. While the current implementation of ST-HMI provides relative stiffness (i.e, stiffness of inclusion/tumors with respect to the background/healthy tissue), shear wave-based methods provide quantitative mechanical parameters. Despite this limitation, ST-HMI may have three advantages over shear wave methods. First, ST-HMI interrogates mechanical properties at the ARF-ROE immediately following the ARF excitation. Therefore, the displacement will be less distorted by tissue heterogeneity and reflected shear waves. Second, ST-HMI may support finer resolution of the mechanical properties compared to the shear wave-based method as the shear wave-based methods need a 2-5 mm lateral average kernel whereas ST-HMI interrogates mechanical parameters pixel by pixel basis at the ARF-ROE. Hollender *et al.* showed that the mechanical resolution of ARFI performs better than the shear wave imaging [28]. Third, displacements are greatest at on-axis to ARF excitation and reduced with shear wave propagation due to dispersion and diffraction, thus, ST-HMI may assess mechanical properties in deeper organs, obese patients, and/or stiffer tissues. Systematically comparing ST-HMI to shear wave-based methods in terms of mechanical resolution, performance in heterogeneous media, and the maximum focal depth are topics of ongoing studies.

The relative stiffness in ST-HMI was generated by normalizing the P2PD image by a profile estimated in the homogeneous region of the image. The normalization profile can be generated from separate measurements in the experimental or *in silico* phantoms as it was done for ARFI displacement images [56]. To quantify the stiffness from the displacement, knowledge of force magnitude is needed. Note, displacement is proportional to the force magnitude. The ARF magnitude (F) is given by $F = 2\alpha I/c$ [17] where α = acoustic attenuation, I = time average intensity, and c = speed of sound. A look-up table or machine learning [57] based approach can be devised to quantify stiffness from the P2PD with the knowledge of α, I, and c in the imaged tissue.

Besides the estimation of the mechanical properties, the beam sequence to generate a 2-D image is fundamentally different between ST-HMI versus HSWI [40]. In HSWI, a 2-D image is formed by tracking harmonic motion using plane-wave away from the ARF-ROE. But in ST-HMI, harmonic motion is tracked at the ARF-ROE and a 2-D image is formed by electronically translating both excitation and tracking beams across the lateral field (Fig. 3). The lateral FOV is fixed to 20 mm for the L7-4 transducer to generate excitation and tracking beam F-number of 2.25 and 1.75 at the focal depth of 30 mm using 44 and 57 transducer elements, respectively. Note, the tracking pulse F-number has to be lower than the excitation pulse F-number to reduce jitter and displacement underestimation [58]. As the 57 elements were used to generate one RF-line, the FOV was smaller than the transducer aperture (Fig. 3). For focusing above 30 mm, the lateral FOV can be larger than 20 mm. However, lateral FOV was kept to 20 mm throughout all experiments for the L7-4 transducer so that the phantom and human images had the same lateral FOV irrespective of the focal depth. There is a tradeoff between the selection of F-number and FOV size. Higher F-number will have higher FOV with lower intensity pulse (i.e., lower displacement) or vice versa. To have displacement above the Cramer-Rao Lower Bound [59], the FOV for L7-4 was fixed to 20 mm which enabled us to use an F-number of 1.75 at a focal depth of 30 mm in this work. However, the F-number can be changed depending on the depth and imaging organ to have a larger FOV. Another way to increase the FOV is to use a transducer with a larger aperture.

This study demonstrates the initial feasibility of ST-HMI by experimenting in the commercially available phantoms, breast

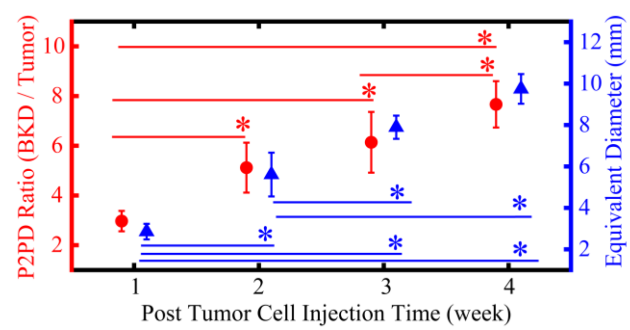

Fig 13: Peak-to-peak (P2PD) displacement ratio of the healthy tissue (BKD) to the tumor (red, left y-axis) and tumor diameter (blue, right y-axis) as a function of time after tumor cell injection. Data are plotted as median ± 05*inter-quartile range over 4 mice. The Kruskal–Wallis test suggests both P2PD ratio and diameter were statistically different across time points. Asterisk (*) represents statistically significant P2PD ratios and diameters between two imaging time points.

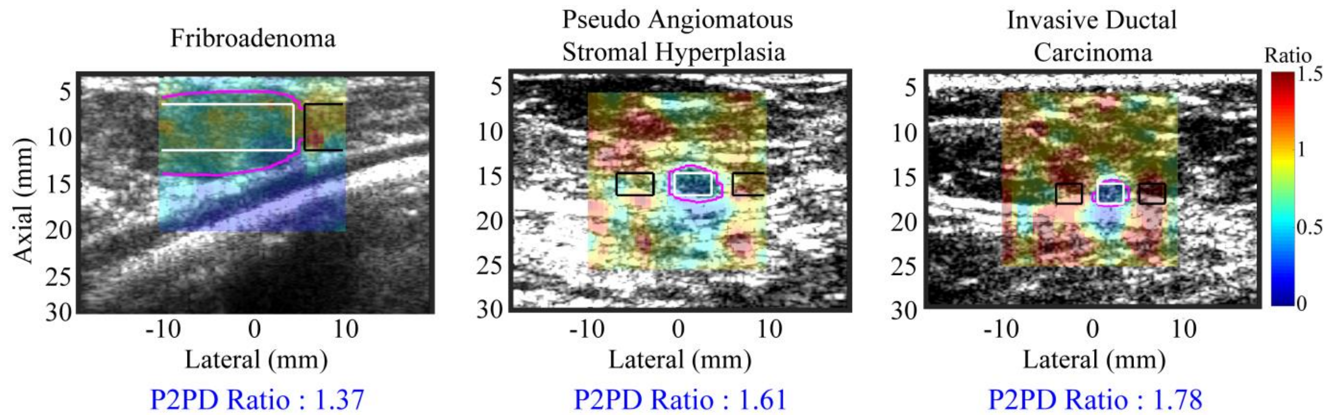

Fig. 14: Normalized peak-to-peak displacements (P2PD) image overlaid on the B-mode ultrasound image of patients with Fibroadenoma, pseudo angiomatous stromal hyperplasia, and invasive ductal carcinoma with respective median P2PD ratio of non-cancerous tissue over tumor at the bottom. Magenta, black and white contours represent tumor boundary, region of interest (ROI) in the non-cancerous tissue, and ROI in the tumor, respectively.

cancer mouse model, and patients with breast masses. The ST-HMI-derived P2PD images contrasted 8, 10, 14, 15, 20, 40, and 60 kPa inclusions embedded in 5 kPa background (Fig. 7). The normalized P2PD values were different between left versus right background ROI of a 10 kPa inclusion (Fig. 7). Quantitatively, the difference in median normalized P2PD in left versus right ROI was 0.12 (1.08-0.96) which was very small. This may be due to a slight difference in Young's modulus of the left versus right background. Note, the manufacturer provided Young's modulus of background is 5 ± 1 kPa. Though inclusions with 10 ± 1 mm diameter were targeted to image, the perceived size varied between inclusions. This may be due to the difference in transducer pressure on the surface of phantoms during imaging, use of the same oscillation frequency, and/or difference in true sizes. However, the perceived size was within the manufacturer-provided error range.

The P2PD ratio increased with Young's moduli ratio with R^2 = 0.93 (Fig. 8(b)). Linear regression was used to derive the R^2. The relationship between the ST-HMI-derived P2PD ratio and Young's moduli ratio may not be linear. In a purely elastic material with point force, the relationship is expected to be linear. However, complex inertia due to 3-D volumetric ARF [21] and the presence of viscosity [31] may render the relationship non-linear. The manufacturer-provided nominal median Young's modulus was used to calculate the R^2 value. The R^2 value may increase if the correct relationship and Young's modulus are used. In addition to high correlation, the ST-HMI-derived contrast and CNR were statistically different between all pairs of inclusions which suggests that the ST-HMI can distinguish two inclusions when the minimum stiffness difference was 16.6% (12 versus 15 kPa). However, this minimum distinction was based on the nominal Young's modulus provided by the manufacturer. The ST-HMI detectability of inclusion can be improved by selecting an optimal frequency as the contrast and CNR of the ST-HMI-derived images depend on the oscillation frequency (Figs. 9 and 10).

Fig. 9 indicates that the perceived size of the inclusion in the ST-HMI images depends on the oscillation frequency because the wavelength of generated shear waves within the ARF excitation beam depends on the oscillation frequency and stiffness (i.e. shear wave speed). In a material with fixed stiffness, the wavelength will be higher for lower frequency and it will average over a larger area that leads to a higher perceived size of the inclusion for lower frequency. For a fixed oscillation, the wavelength will be larger for the stiffer materials (i.e., higher shear wave speed). As a result, the perceived size will be larger in a stiffer material for a fixed oscillation. As an example at 180 Hz oscillation frequency, the perceived size was similar to the true size of 15 kPa inclusion whereas the perceived size was higher than the true size of 60 kPa inclusion (Fig. 9). Note, the ST-HMI interrogates mechanical properties at the ARF-ROE without observing shear wave propagation away from the ARF-ROE. Therefore, the impact of oscillation on the perceived size of inclusions was observed mainly in the axial direction. There was not much distortion of inclusion's boundary in the lateral direction except for 60 Hz. A similar impact of frequency on the perceived size of inclusions was observed in the shear wave derived local phase velocity images [60], [61]. Note, the oscillation frequencies from 60 to 420 Hz were used to interrogate 15 and 60 kPa inclusions. The oscillation frequency lower or higher than this range can be achieved in ST-HMI. The minimum oscillation frequency will be limited by the ultrasound system's capability to quickly charge the power supply and transducer's durability to withstand long excitation pulses. However, the tracking pulse PRF and the number of excitation pulses per cycle will define the maximum oscillation frequency. The Nyquist rate will limit the minimum number of excitation pulses per cycle. For example, a minimum of 2 excitation pulses per cycle is needed to construct a 1000 Hz oscillation frequency. However, the excitation pulses higher than the limit set by the Nyquist rate may be needed for better realization of the oscillation. The maximum oscillation frequency of 1000 Hz can be attainable with 3 excitation pulses per cycle and a PRF of 10 kHz. Future work will explore the use of multi-frequency oscillation with a higher frequency range to achieve maximum contrast and CNR.

Other parameters such as excitation pulse duty cycle, cycle number, and excitation pulse offset did not have a larger impact

This article has been accepted for publication in a future issue of this journal, but has not been fully edited. Content may change prior to final publication. Citation information: DOI 10.1109/TMI.2021.3055779, IEEE Transactions on Medical Imaging

on CNR and contrast as the oscillation frequency. The median percent change in contrast and CNR was under 1% when duty cycle, cycle number, and excitation pulse offset were greater than 6.36%, 6, and 0 ms, respectively. These results are meaningful as they indicate that it is possible to perform ST-HMI with low exposure to ARF without compromising its performance. It will aid to implement the ST-HMI in low-cost ultrasound systems, which cannot generate a longer excitation pulse due to memory and/or power supply constraints. Note, the CNR and contrast were calculated based on the inclusion's boundary derived from the B-mode image. Even though inclusion and background are isoechoic, there is a slight change in the echogenicity at the boundary which guides us to draw the boundary (arrowhead in Fig.5a). However, the change in echogenicity was not present in the entire inclusion's circumference. An approximate circle was drawn based on the visible change in the echogenicity in the boundary. The derivation of the boundary from the B-mode images may bias the calculation of CNR and contrast. However, the same inclusion boundary was used to compare ST-HMI versus ARFI and investigate the impact of oscillation frequency, excitation pulse per cycle, oscillation pulse number, and excitation pulse offset on the ST-HMI images.

These results in the phantoms are very promising. However, phantoms are the idealistic representation of tissues. *In vivo* performance of ST-HMI was evaluated by monitoring longitudinal changes in stiffness of mouse breast cancer and human breast masses. The perceived tumor's boundaries in the ST-HMI images did not always match (2nd and 4th column in Fig. 12) with the boundary derived from the B-mode ultrasound images (magenta contour in Fig. 12). It may be due to the heterogeneous nature of the tumor which may be yielded to heterogenous P2PD values in tumors. Note, it has been demonstrated that the stiffness of the tumor depends on its composition (fibrosis, necrosis, or cellular tissue) [62]. The P2PD in the background below the tumor was lower than the background beside the tumor. It may be due to the difference in composition of the background below versus beside the tumor. The tumor may be also highly attenuating. The higher attenuation reduced the ARF magnitude below the tumor which may be resulted in lower P2PD values. Future studies will compare the heterogeneity of ST-HMI-derived P2PD values of tumor and background with the histopathological findings and correct for the attenuation difference between background and tumor.

Both Figs. 12 and 13 indicate that mouse tumors became stiffer compared to the nearest non-cancerous tissues over time, with the cancerous cells ingression. Previously, it has been demonstrated in the xenograft breast cancer mouse model that shear wave derived elasticity increases with tumor growth [62], [63] and Chamming *et. al* [62] found an excellent correlation between tumor elasticity versus maximum diameter with a correlation coefficient of 0.94. In this study, the Pearson correlation coefficient between median P2PD ratio versus median diameter over mice (N=4) was 0.99 ($p < 0.05$). However, after considering each mouse separately (mice # 4, time points # 4, N=16), the Pearson correlation coefficient between P2PD ratio versus diameter was 0.82 ($p < 0.05$). The discrepancy in the correlation coefficient may be due to the mismatch between the imaging plane at different time points. As a 2-D slice of a 3-D tumor volume was imaged, the plane with maximum tumor diameter may not be imaged at each time point.

To the best of our knowledge, this study is the first *in vivo* study to use a high-frequency (15.63 MHz) ultrasound array (L22-14vXLF) for both generating ARF and tracking ARF-induced motion. The aperture size of the L22-14vXLF was 12 mm which is smaller than the 38 mm aperture size of the L7-4 transducer. Similar to L7-4, the excitation and tracking pulse F-numbers were fixed to 2.25 and 1.75, respectively which resulted in approximately 4.2 mm lateral FOV in the L22-14vXLF-generated images. The 4.2 mm lateral FOV contained 14 RF-lines that were acquired using electronic translation. Therefore, the ST-HMI working principle thus still holds for L22-14vXLF-generated images. However, if the tumor was larger than 3 mm, the transducer was mechanically translated to cover both the tumor and surrounding tissues. The performance of ST-HMI can be improved for small animal imaging by using a different high-frequency transducer with a larger aperture. The P2PD ratio was not able to statistically distinguish between 2nd versus 3rd week and 3rd versus 4th week. This might be due to the small number of mice used in the study (N = 4). As the lateral FOV of the ST-HMI image using L22-14vXLF was 4 mm, acquisitions at different locations were stitched together to form the final image which may introduce some errors. As the normalizing profile was generated from the homogeneous non-cancerous tissues, the normalization process may induce errors if there is no healthy tissue (axial depth of around 8-11 mm). To solve this problem, we extrapolated the normalizing profile by fitting it to a Gaussian function. It may still induce some errors. That's why the ROI in the tumor was selected to match the available depth in the healthy tissue instead of the whole tumor. Finally, in the clinical study, ST-HMI detected three different types of breast masses and showed that the malignant breast mass (IDC) was stiffer than the benign breast masses (FA and PASH) with respect to the nearest non-cancerous tissues. Previous ultrasound elastography based studies showed that malignant breast tumors are stiffer than benign tumors [64] [7], [65]. However, more patients are needed to confirm similar findings using ST-HMI. The normalized P2PD values of non-cancerous healthy tissues were not homogeneous and the normalized P2PD values in the non-cancerous tissue ROI (black contour) of the IDC patients were greater than one. It may be due to the inherent heterogeneity in breast tissue composition. The breast consists of fibroglandular tissue, fatty tissue, milk ducts, milk glands, and blood vessels with varying mechanical properties. The inhomogeneity of ST-HMI images may be due to the inherent inhomogeneity of the breast tissue that is needed to be confirmed. Future studies will validate the ST-HMI findings with the histopathological findings of the excised post-surgery human breast specimen [64].

This feasibility study of ST-HMI demonstrated very promising results. However, the study has three main limitations. First, P2PD displacements were used to infer the mechanical properties. However, displacement is a function of both elasticity and viscosity [31], [33]. Second, the P2PD ratio of non-cancerous tissue to the tumor was used to account for patients to patients or mice to mice variation in the ARF amplitude. The mechanical property assessments will be confounded if the non-cancerous tissues experienced different force amplitudes than the tumor or the mechanical properties of non-cancerous tissues change over time. Third, the mechanical anisotropy of breast tissue [66] was ignored. The mechanical anisotropy may confound the displacement measurements [42], [43], [67]. Future investigations will address these limitations.

V. Conclusion

In this study, the initial feasibility of generating and tracking harmonic motion at the ARF-ROE was shown using a linear array transducer. ST-HMI contrasted six inclusions with varying stiffness using two commercially available phantoms. In the preclinical mouse study, the P2PD ratio of the non-cancerous tissue to the tumor increased over time indicating that the tumor was stiffening during growth. In the clinical application, ST-HMI detected three different types of breast masses and showed that the malignant breast mass (IDC) was stiffer than the benign breast masses (FA and PASH) with respect to the nearest non-cancerous tissues. These results indicate that ST-HMI is feasible and can assess the mechanical properties of tissue via harmonic motion generation and tracking at ARF-ROE without observing shear wave propagation.

Acknowledgment

The authors thank Drs. Saurabh Singh, Indranil Basu, and Chandan Guha from the Albert Einstein College of Medicine & Montefiore Medical Center, Bronx, NY USA for providing the cancer cell for the mouse study and Rachel Weber, Drs. Bret Taback, and Richard Ha for the help in collecting patient's data.

References

[1] R. M. S. Sigrist, J. Liau, A. El Kaffas, M. C. Chammas, and J. K. Willmann, "Ultrasound Elastography: Review of Techniques and Clinical Applications," *Theranostics*, vol. 7, no. 5, pp. 1303–1329, 2017, doi: 10.7150/thno.18650.

[2] S. K. Venkatesh *et al.*, "Magnetic resonance elastography: beyond liver fibrosis—a case-based pictorial review," *Abdom. Radiol.*, vol. 43, no. 7, pp. 1590–1611, Jul. 2018, doi: 10.1007/s00261-017-1383-1.

[3] S. Wang and K. V. Larin, "Optical coherence elastography for tissue characterization: a review," *J. Biophotonics*, vol. 8, no. 4, pp. 279–302, Apr. 2015, doi: 10.1002/jbio.201400108.

[4] K. Nightingale *et al.*, "Derivation and analysis of viscoelastic properties in human liver: Impact of frequency on fibrosis and steatosis staging," *IEEE Trans. Ultrason. Ferroelectr. Freq. Control*, vol. 62, no. 1, pp. 165–175, 2015, doi: 10.1109/TUFFC.2014.006653.

[5] S. Chen *et al.*, "Assessment of liver viscoelasticity by using shear waves induced by ultrasound radiation force.," *Radiology*, vol. 266, no. 3, pp. 964–70, Mar. 2013, doi: 10.1148/radiol.12120837.

[6] Y. Zhu *et al.*, "The Role of Viscosity Estimation for Oil-in-gelatin Phantom in Shear Wave Based Ultrasound Elastography," *Ultrasound Med. Biol.*, vol. 41, no. 2, pp. 601–609, Feb. 2015, doi: 10.1016/j.ultrasmedbio.2014.09.028.

[7] V. Kumar *et al.*, "Viscoelastic parameters as discriminators of breast masses: Initial human study results.," *PLoS One*, vol. 13, no. 10, p. e0205717, 2018, doi: 10.1371/journal.pone.0205717.

[8] J. Zhan, J.-M. Jin, X.-H. Diao, and Y. Chen, "Acoustic radiation force impulse imaging (ARFI) for differentiation of benign and malignant thyroid nodules—A meta-analysis," *Eur. J. Radiol.*, vol. 84, no. 11, pp. 2181–2186, Nov. 2015, doi: 10.1016/j.ejrad.2015.07.015.

[9] J. M. Correas *et al.*, "Prostate cancer: Diagnostic performance of real-time shear-wave elastography," *Radiology*, vol. 275, no. 1, pp. 280–289, Apr. 2015, doi: 10.1148/radiol.14140567.

[10] Z. Wang, H. Yang, C. Suo, J. Wei, R. Tan, and M. Gu, "Application of Ultrasound Elastography for Chronic Allograft Dysfunction in Kidney Transplantation," *J. Ultrasound Med.*, vol. 36, no. 9, pp. 1759–1769, Sep. 2017, doi: 10.1002/jum.14221.

[11] M. M. Hossain *et al.*, "Evaluating Renal Transplant Status Using Viscoelastic Response (VisR) Ultrasound.," *Ultrasound Med. Biol.*, vol. 44, no. 8, pp. 1573–1584, May 2018, doi: 10.1016/j.ultrasmedbio.2018.03.016.

[12] J. E. Brandenburg *et al.*, "Ultrasound elastography: the new frontier in direct measurement of muscle stiffness.," *Arch. Phys. Med. Rehabil.*, vol. 95, no. 11, pp. 2207–19, Nov. 2014, doi: 10.1016/j.apmr.2014.07.007.

[13] M. S. Taljanovic *et al.*, "Shear-Wave Elastography: Basic Physics and Musculoskeletal Applications," *RadioGraphics*, vol. 37, no. 3, pp. 855–870, May 2017, doi: 10.1148/rg.2017160116.

[14] T. J. Czernuszewicz *et al.*, "Performance of acoustic radiation force impulse ultrasound imaging for carotid plaque characterization with histologic validation," *J. Vasc. Surg.*, vol. 66, no. 6, pp. 1749-1757.e3, Dec. 2017, doi: 10.1016/j.jvs.2017.04.043.

[15] D. Marlevi *et al.*, "Combined spatiotemporal and frequency-dependent shear wave elastography enables detection of vulnerable carotid plaques as validated by MRI," *Sci. Rep.*, vol. 10, no. 1, p. 403, Dec. 2020, doi: 10.1038/s41598-019-57317-7.

[16] A. J. Collins *et al.*, "'United States Renal Data System 2011 Annual Data Report: Atlas of chronic kidney disease & end-stage renal disease in the United States.," *Am. J. Kidney Dis.*, vol. 59, no. 1 Suppl 1, pp. A7, e1-420, Jan. 2012, doi: 10.1053/j.ajkd.2011.11.015.

[17] J. R. Doherty, G. E. Trahey, K. R. Nightingale, and M. L. Palmeri, "Acoustic radiation force elasticity imaging in diagnostic ultrasound.," *IEEE Trans. Ultrason. Ferroelectr. Freq. Control*, vol. 60, no. 4, pp. 685–701, Apr. 2013, doi: 10.1109/TUFFC.2013.2617.

[18] K. Nightingale, M. S. Soo, R. Nightingale, and G. Trahey, "Acoustic radiation force impulse imaging: in vivo demonstration of clinical feasibility.," *Ultrasound Med. Biol.*, vol. 28, no. 2, pp. 227–35, Feb. 2002, Accessed: Dec. 07, 2014. [Online]. Available: http://www.ncbi.nlm.nih.gov/pubmed/11937286.

[19] M. M. Hossain *et al.*, "Viscoelastic Response Ultrasound Detects Changes in Degree of Mechanical Anisotropy with Renal Fibrosis in Pig Model," in *2019 IEEE International Ultrasonics Symposium (IUS)*, Oct. 2019, vol. 2019-Octob, pp. 415–418, doi: 10.1109/ULTSYM.2019.8925733.

[20] E. E. Konofagou and K. Hynynen, "Localized harmonic motion imaging: Theory, simulations and experiments," *Ultrasound Med. Biol.*, vol. 29, no. 10, pp. 1405–1413, 2003, doi: 10.1016/S0301-5629(03)00953-0.

[21] M. R. Selzo, C. J. Moore, M. M. Hossain, M. L. Palmeri, and C. M. Gallippi, "On the Quantitative Potential of Viscoelastic Response (VisR) Ultrasound Using the One-Dimensional Mass-Spring-Damper Model.," *IEEE Trans. Ultrason. Ferroelectr. Freq. Control*, vol. 63, no. 9, pp. 1276–87, 2016, doi: 10.1109/TUFFC.2016.2539323.

[22] A. P. Sarvazyan, O. V. Rudenko, S. D. Swanson, J. B. Fowlkes, and S. Y. Emelianov, "Shear wave elasticity imaging: a new ultrasonic technology of medical diagnostics.," *Ultrasound Med. Biol.*, vol. 24, no. 9, pp. 1419–35, Nov. 1998, doi: 10.1016/j.ultrasmedbio.2010.05.015.

[23] K. Nightingale, S. McAleavey, and G. Trahey, "Shear-wave generation using acoustic radiation force: in vivo and ex vivo results.," *Ultrasound Med. Biol.*, vol. 29, no. 12, pp. 1715–1723, Dec. 2003, doi: 10.1016/j.ultrasmedbio.2003.08.008.

[24] P. Song, H. Zhao, A. Manduca, M. W. Urban, J. F. Greenleaf, and S. Chen, "Comb-Push Ultrasound Shear Elastography (CUSE): A Novel Method for Two-Dimensional Shear Elasticity Imaging of Soft Tissues," *IEEE Trans. Med. Imaging*, vol. 31, no. 9, pp. 1821–1832, Sep. 2012, doi: 10.1109/TMI.2012.2205586.

[25] J. Bercoff, M. Tanter, and M. Fink, "Supersonic shear imaging: a new technique for soft tissue elasticity mapping.," *IEEE Trans. Ultrason. Ferroelectr. Freq. Control*, vol. 51, no. 4, pp. 396–409, Apr. 2004,

doi: 10.1109/TUFFC.2004.1295425.

[26] J. Vappou, C. Maleke, and E. E. Konofagou, "Quantitative viscoelastic parameters measured by harmonic motion imaging," *Phys. Med. Biol.*, vol. 54, no. 11, pp. 3579–3594, Jun. 2009, doi: 10.1088/0031-9155/54/11/020.

[27] C. Amador Carrascal, S. Chen, M. W. Urban, and J. F. Greenleaf, "Acoustic Radiation Force-Induced Creep–Recovery (ARFICR): A Noninvasive Method to Characterize Tissue Viscoelasticity," *IEEE Trans. Ultrason. Ferroelectr. Freq. Control*, vol. 65, no. 1, pp. 3–13, Jan. 2018, doi: 10.1109/TUFFC.2017.2768184.

[28] P. J. Hollender, S. J. Rosenzweig, K. R. Nightingale, and G. E. Trahey, "Single- and Multiple-Track-Location Shear Wave and Acoustic Radiation Force Impulse Imaging: Matched Comparison of Contrast, Contrast-to-Noise Ratio and Resolution," *Ultrasound Med. Biol.*, vol. 41, no. 4, pp. 1043–1057, 2015, doi: 10.1016/j.ultrasmedbio.2014.11.006.

[29] Y. S. Cho, S. Lim, Y. Kim, T. Y. Kim, W. K. Jeong, and J. H. Sohn, "Abdominal Wall Thickness Affects Liver Stiffness Measurements by 2-D Shear Wave Elastography in Patients with Chronic Liver Disease," *Ultrasound Med. Biol.*, vol. 00, no. 00, pp. 1–7, Jul. 2019, doi: 10.1016/j.ultrasmedbio.2019.06.415.

[30] X. Zhao and A. a. Pelegri, "Dynamic Simulation of Viscoelastic Soft Tissue in Acoustic Radiation Force Creep Imaging," *J. Biomech. Eng.*, vol. 136, no. 9, p. 094502, 2014, doi: 10.1115/1.4027934.

[31] M. M. Hossain and C. M. Gallippi, "Viscoelastic Response Ultrasound Derived Relative Elasticity and Relative Viscosity Reflect True Elasticity and Viscosity: In Silico and Experimental Demonstration.," *IEEE Trans. Ultrason. Ferroelectr. Freq. Control*, vol. 67, no. 6, pp. 1102–1117, 2020, doi: 10.1109/TUFFC.2019.2962789.

[32] M. Hossain, C. Moore, and C. Gallippi, "On the quantitative potential of Viscoelastic Response (VisR) ultrasound using matrix array transducers: In silico demonstration," in *2016 IEEE International Ultrasonics Symposium (IUS)*, Sep. 2016, vol. 63, no. 9, pp. 1–4, doi: 10.1109/ULTSYM.2016.7728878.

[33] M. M. Hossain, T. Nichols, E. Merricks, and C. Gallippi, "Viscoelastic response (VisR)-derived relative elasticity and relative viscosity reflect tissue elasticity and viscosity: In silico and experimental demonstration in liver," in *2017 IEEE International Ultrasonics Symposium (IUS)*, Sep. 2017, no. 2, pp. 1–1, doi: 10.1109/ULTSYM.2017.8091807.

[34] T. Payen *et al.*, "Elasticity mapping of murine abdominal organs in vivo using harmonic motion imaging (HMI)," *Phys. Med. Biol.*, vol. 61, no. 15, pp. 5741–5754, Aug. 2016, doi: 10.1088/0031-9155/61/15/5741.

[35] T. Payen *et al.*, "Harmonic Motion Imaging of Pancreatic Tumor Stiffness Indicates Disease State and Treatment Response," *Clin. Cancer Res.*, vol. 26, no. 6, pp. 1297–1308, Mar. 2020, doi: 10.1158/1078-0432.CCR-18-3669.

[36] C. Wu *et al.*, "Assessing Age-Related Changes in the Biomechanical Properties of Rabbit Lens Using a Coaligned Ultrasound and Optical Coherence Elastography System," *Invest. Ophthalmol. Vis. Sci.*, vol. 56, no. 2, pp. 1292–1300, Feb. 2015, doi: 10.1167/iovs.14-15654.

[37] Y. Han, S. Wang, T. Payen, and E. Konofagou, "Fast lesion mapping during HIFU treatment using harmonic motion imaging guided focused ultrasound (HMIgFUS) in vitro and in vivo," *Phys. Med. Biol.*, vol. 62, no. 8, pp. 3111–3123, Apr. 2017, doi: 10.1088/1361-6560/aa6024.

[38] J. Grondin, T. Payen, S. Wang, and E. E. Konofagou, "Real-time monitoring of high intensity focused ultrasound (HIFU) ablation of in vitro canine livers using harmonic motion imaging for focused ultrasound (HMIFU)," *J. Vis. Exp.*, vol. 2015, no. 105, pp. 1–7, Nov. 2015, doi: 10.3791/53050.

[39] S. Chen *et al.*, "Shearwave dispersion ultrasound vibrometry (SDUV) for measuring tissue elasticity and viscosity.," *IEEE Trans. Ultrason. Ferroelectr. Freq. Control*, vol. 56, no. 1, pp. 55–62, Jan. 2009, doi: 10.1109/TUFFC.2009.1005.

[40] S. Sadeghi, C.-Y. Lin, and D. H. Cortes, "Narrowband Shear Wave Generation Using Sinusoidally Modulated Acoustic Radiation Force," *IEEE Trans. Ultrason. Ferroelectr. Freq. Control*, vol. 66, no. 2, pp. 264–272, Feb. 2019, doi: 10.1109/TUFFC.2018.2884847.

[41] D. M. Dumont, J. R. Doherty, and G. E. Trahey, "Noninvasive assessment of wall-shear rate and vascular elasticity using combined ARFI/SWEI/Spectral doppler imaging system," *Ultrason. Imaging*, vol. 33, no. 3, pp. 165–188, Jul. 2011, doi: 10.1177/016173461103300302.

[42] M. M. Hossain *et al.*, "Mechanical Anisotropy Assessment in Kidney Cortex Using ARFI Peak Displacement: Preclinical Validation and Pilot In Vivo Clinical Results in Kidney Allografts.," *IEEE Trans. Ultrason. Ferroelectr. Freq. Control*, vol. 66, no. 3, pp. 551–562, Mar. 2019, doi: 10.1109/TUFFC.2018.2865203.

[43] M. M. Hossain and C. M. Gallippi, "Electronic Point Spread Function Rotation Using a Three-row Transducer for ARFI-Based Elastic Anisotropy Assessment: In Silico and Experimental Demonstration.," *IEEE Trans. Ultrason. Ferroelectr. Freq. Control*, vol. PP, no. c, pp. 1–1, Aug. 2020, doi: 10.1109/TUFFC.2020.3019002.

[44] M. M. Hossain *et al.*, "In vivo mechanical anisotropy assessment in renal cortex using ARFI peak displacement," in *2017 IEEE International Ultrasonics Symposium (IUS)*, Sep. 2017, vol. 64, no. 6, pp. 1–4, doi: 10.1109/ULTSYM.2017.8092413.

[45] K. A. Skalina, S. Singh, C. G. Chavez, F. Macian, and C. Guha, "Low Intensity Focused Ultrasound (LOFU)-mediated Acoustic Immune Priming and Ablative Radiation Therapy for in situ Tumor Vaccines.," *Sci. Rep.*, vol. 9, no. 1, p. 15516, 2019, doi: 10.1038/s41598-019-51332-4.

[46] T. Savage, S. Pandey, and C. Guha, "Postablation Modulation after Single High-Dose Radiation Therapy Improves Tumor Control via Enhanced Immunomodulation," *Clin. Cancer Res.*, vol. 26, no. 4, pp. 910–921, Feb. 2020, doi: 10.1158/1078-0432.CCR-18-3518.

[47] G. Montaldo, M. Tanter, J. Bercoff, N. Benech, and M. Fink, "Coherent plane-wave compounding for very high frame rate ultrasonography and transient elastography.," *IEEE Trans. Ultrason. Ferroelectr. Freq. Control*, vol. 56, no. 3, pp. 489–506, Mar. 2009, doi: 10.1109/TUFFC.2009.1067.

[48] G. F. Pinton, J. J. Dahl, and G. E. Trahey, "Rapid tracking of small displacements with ultrasound.," *IEEE Trans. Ultrason. Ferroelectr. Freq. Control*, vol. 53, no. 6, pp. 1103–17, Jun. 2006, doi: 10.1109/ULTSYM.2005.1603285.

[49] D. M. Giannantonio, D. M. Dumont, G. E. Trahey, and B. C. Byram, "Comparison of physiological motion filters for in vivo cardiac ARFI.," *Ultrason. Imaging*, vol. 33, no. 2, pp. 89–108, Apr. 2011, doi: 10.1177/016173461103300201.

[50] K. Nightingale, M. Palmeri, and G. Trahey, "Analysis of contrast in images generated with transient acoustic radiation force.," *Ultrasound Med. Biol.*, vol. 32, no. 1, pp. 61–72, Jan. 2006, doi: 10.1016/j.ultrasmedbio.2005.08.008.

[51] A. Manduca *et al.*, "Magnetic resonance elastography: Non-invasive mapping of tissue elasticity," *Med. Image Anal.*, vol. 5, no. 4, pp. 237–254, Dec. 2001, doi: 10.1016/S1361-8415(00)00039-6.

[52] J. Guo, S. Hirsch, M. Scheel, J. Braun, and I. Sack, "Three-parameter shear wave inversion in MR elastography of incompressible transverse isotropic media: Application to in vivo lower leg muscles," *Magn. Reson. Med.*, vol. 75, no. 4, pp. 1537–1545, Apr. 2016, doi: 10.1002/mrm.25740.

[53] Y. Zheng, S. G. Chen, W. Tan, R. Kinnick, and J. F. Greenleaf, "Detection of tissue harmonic motion induced by ultrasonic radiation force using pulse-echo ultrasoundand Kalman filter," *IEEE Trans. Ultrason. Ferroelectr. Freq. Control*, vol. 54, no. 2, pp. 290–300, 2007, doi: Doi 10.1109/Tuffc.2007.243.

[54] M. W. Urban, S. Chen, and J. Greenleaf, "Harmonic motion detection in a vibrating scattering medium.," *IEEE Trans. Ultrason. Ferroelectr. Freq. Control*, vol. 55, no. 9, pp. 1956–74, Sep. 2008, doi: 10.1109/TUFFC.887.

[55] R. H. Behler, T. C. Nichols, E. P. Merricks, and C. M. Gallippi, "A Rigid Wall Approach to Physiologic Motion Rejection in Arterial Radiation Force Imaging," in *2007 IEEE Ultrasonics Symposium Proceedings*, Oct. 2007, pp. 359–364, doi: 10.1109/ULTSYM.2007.100.

[56] P. Hollender, S. Noor, D. Bradway, and G. Trahey, "Force-Map Normalization for ARFI Imaging," in *2019 IEEE International Ultrasonics Symposium (IUS)*, Oct. 2019, vol. 2019-Octob, pp. 411–414, doi: 10.1109/ULTSYM.2019.8926049.

[57] C. J. Moore *et al.*, "Texture in Quantitative Viscoelastic Response (QVisR) Images Differentiates Dystrophic from Control Skeletal Muscles in Boys, In Vivo," in *2019 IEEE International Ultrasonics Symposium (IUS)*, Oct. 2019, vol. 2019-Octob, pp. 2145–2147, doi: 10.1109/ULTSYM.2019.8925927.

[58] M. L. Palmeri, S. a. McAleavey, G. E. Trahey, and K. R. Nightingale, “Ultrasonic tracking of acoustic radiation force-induced displacements in homogeneous media,” *IEEE Trans. Ultrason. Ferroelectr. Freq. Control*, vol. 53, no. 7, pp. 1300–1313, 2006, doi: 10.1109/TUFFC.2006.1665078.

[59] W. F. Walker and G. E. Trahey, “A Fundamental Limit on Delay Estimation Using Partially Correlated Speckle Signals,” *IEEE Trans. Ultrason. Ferroelectr. Freq. Control*, vol. 42, no. 2, pp. 301–308, 1995.

[60] P. Kijanka and M. W. Urban, “Local Phase Velocity Based Imaging: A New Technique Used for Ultrasound Shear Wave Elastography.,” *IEEE Trans. Med. Imaging*, vol. 38, no. 4, pp. 894–908, Apr. 2019, doi: 10.1109/TMI.2018.2874545.

[61] Y. Han, S. Wang, H. Hibshoosh, B. Taback, and E. Konofagou, “Tumor characterization and treatment monitoring of postsurgical human breast specimens using harmonic motion imaging (HMI),” *Breast Cancer Res.*, vol. 18, no. 1, pp. 1–11, 2016, doi: 10.1186/s13058-016-0707-3.

[62] F. Chamming’s *et al.*, “Shear wave elastography of tumour growth in a human breast cancer model with pathological correlation.,” *Eur. Radiol.*, vol. 23, no. 8, pp. 2079–86, Aug. 2013, doi: 10.1007/s00330-013-2828-8.

[63] F. Chamming’s *et al.*, “Supersonic Shear Wave Elastography of Response to Anti-cancer Therapy in a Xenograft Tumor Model.,” *Ultrasound Med. Biol.*, vol. 42, no. 4, pp. 924–30, Apr. 2016, doi: 10.1016/j.ultrasmedbio.2015.12.001.

[64] N. Saharkhiz *et al.*, “Harmonic motion imaging of human breast masses: an in vivo clinical feasibility.,” *Sci. Rep.*, vol. 10, no. 1, p. 15254, Sep. 2020, doi: 10.1038/s41598-020-71960-5.

[65] X. Zheng *et al.*, “Shear-Wave Elastography of the Breast: Added Value of a Quality Map in Diagnosis and Prediction of the Biological Characteristics of Breast Cancer.,” *Korean J. Radiol.*, vol. 21, no. 2, pp. 172–180, 2020, doi: 10.3348/kjr.2019.0453.

[66] K. Skerl, S. Vinnicombe, K. Thomson, D. McLean, E. Giannotti, and A. Evans, “Anisotropy of Solid Breast Lesions in 2D Shear Wave Elastography is an Indicator of Malignancy,” *Acad. Radiol.*, vol. 23, no. 1, pp. 53–61, Jan. 2016, doi: 10.1016/j.acra.2015.09.016.

[67] M. Hossain, C. J. Moore, and C. M. Gallippi, “Acoustic Radiation Force Impulse-Induced Peak Displacements Reflect Degree of Anisotropy in Transversely Isotropic Elastic Materials,” *IEEE Trans. Ultrason. Ferroelectr. Freq. Control*, vol. 64, no. 6, pp. 989–1001, Jun. 2017, doi: 10.1109/TUFFC.2017.2690223.